# The Transparent Nucleus: unperturbed inverse kinematics nucleon knockout measurements with a 48 GeV/c carbon beam

(The BM@N Collaboration)

**From superconductors to atomic nuclei, dense strongly-interacting many-body systems are paramount in physics. Measuring the ground-state distribution of particles in such systems is a formidable challenge, that is often met by scattering experiments which reconstruct the initial distribution of knocked-out particles using energy and momentum conservation. However, quantum mechanics imposes a fundamental limitation on interpreting these measurements due to indistinguishable interference of initial- and final-state interactions (ISI/FSI) between the incoming and scattered particles and the residual system [? ]. This is a fundamental limitation for probing the microscopic structure of atomic nuclei. Here we study the ground-state distribution of single nucleons and correlated nucleon pairs in atomic nuclei by scattering 48 GeV/c Carbon-12 ($^{12}$C) ions from hydrogen in quasi-free inverse kinematics and detecting two protons at large angles in coincidence with an intact Boron-11 ($^{11}$B) nucleus. The post-selection of $^{11}$B is shown to exclude the otherwise large ISI/FSI contributions that would break the $^{11}$B apart. In addition, by detecting residual $^{10}$B and $^{10}$Be nuclei, we identified scattering events from short-range correlated (SRC) nucleon-nucleon pairs [1, 2], for the first time in inverse kinematics, and established their factorization [3] from the residual nuclear system. All measured reactions are well described by theoretical calculations that exclude ISI/FSI. Our results thus showcase a new ability to study the short-distance structure of short-lived radioactive atomic nuclei at the forthcoming FAIR and FRIB facilities. These studies will be pivotal for developing a ground-breaking microscopic understanding of nuclei far from stability and of cold dense nuclear systems such as neutron stars.**

By turning off the interactions between atoms in atomic traps and the trap itself, physicists can measure the ground-state properties of strongly interacting atoms in ultra-cold gases [? ]. These systems thus allow exploring a wide range of fundamental quantum mechanical phenomena, imitating strongly correlated states in condensed matter and other systems where one cannot control the interactions [? ].

Constructing such model systems is extremely challenging for atomic nuclei, due to their high-density and complex strong interaction. Instead, physicists scatter electrons from nuclei, knock out single nucleons, and detect the electron and the nucleon with high-resolution detectors. Experiments can then select either the state of the un-detected intact residual nucleus (post-selection) [? ] or the reaction kinematics (pre-selection) to suppress ISI/FSI effects [1].

While largely limited to stable nuclei, such measurements of atomic nuclei helped establish the nuclear shell model [4] and the existence of SRC nucleon pairs [1, 2]. SRCs are pairs of strongly interacting nucleons at short distances. They account for most of the nucleons in the nucleus with momenta above the Fermi-momentum ($k_F$) [5]. These independent pairs are the next approximation after the independent-particle shell model and their study provides insight to properties of dense nuclear matter [? ], the strong nuclear interaction at short distances and high momenta [6], and the role of quarks and gluons in atomic nuclei [1, 7]. The study of SRC pairs in atomic nuclei far from stability, using radioactive-ion beams, is a new frontier of nuclear science.

The fleeting nature of nuclei far from stability requires inverse kinematics, scattering high-energy nuclei from stationary targets. The high-cross-section proton probes have much greater ISI, preventing kinematic pre-selection to reduce ISI/FSI. Post-selection requires direct detection of the residual nuclear system, since the missing-energy resolution is usually insufficient to measure its state indirectly.

Here we use post-selection in high-energy inverse kinematics to probe single-particle states and SRCs in the well understood $^{12}$C nucleus. We selected $^{11}$B fragments after a proton knockout $(p, 2p)$ reaction to successfully study the distribution of protons in the $p$-shell of $^{12}$C. We show, for the first time, that consistent distributions can be obtained using both quasielastic (QE) and inelastic (IE) scattering reactions, which also agree with theoretical calculations. We then use the selection of $^{10}$B and $^{10}$Be fragments to identify, for the first time in inverse kinematics, the hard breakup of SRC pairs. These post-selections eliminate most events, but result in an event sample that is insensitive to ISI/FSI. Thus this opens the gate for studying the single-particle and short-distance structure of nuclei far from stability.

## EXPERIMENTAL SETUP

The experiment took place in 2018 at the Joint Institute for Nuclear Research (JINR), using a 4 GeV/c/nucleon ion beam from the Nuclotron accelerator, a stationary 30 cm long liquid-hydrogen target,

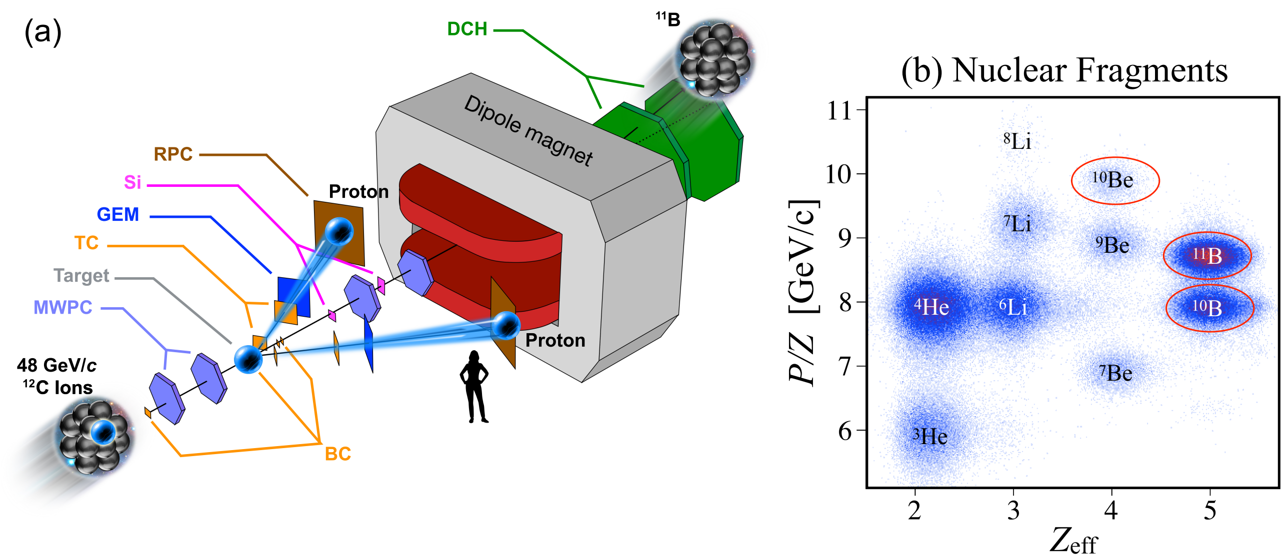


**Fig. 1.** | **Experimental Setup and Fragment Identification.** (a) Carbon nuclei traveling at 48 GeV/c hit protons in a liquid hydrogen target, knocking out individual protons from the beam-ion. Position- and time-sensitive detectors (MWPC, GEM, RPC, Si, and DCH) are used to track the incoming ion beam, knockout protons, and residual nuclear fragments and determine their momenta. (b) The bend of the nuclear fragments in the large dipole magnet, combined with charge measurements with the beam counters (BC) allows identifying the various fragments. In this work we refer to events with detected $^{11}$B, $^{10}$B, and $^{10}$Be heavy fragments, see text for details

and a modified BM@N (Baryonic Matter at Nuclotron) experimental setup, as shown in Fig. 1a.

The beam was monitored before the target using thin scintillator-based beam counters (BCs) and two multi-wire proportional chambers (MWPCs) used for trajectory and charge identification for each event. The BC closer to the target was also used to define the event start time $t_0$.

A two-arm spectrometer (TAS) was placed downstream of the target to detect the two protons from the $(p, 2p)$ reaction that emerge at $24° - 37°$, corresponding to 90° QE scattering in the two-protons center-of-mass (c.m). Each spectrometer arm consisted of scintillator trigger counters (TC), gas electron multiplier (GEM) stations, and multi-gap resistive plate chamber (RPC) walls.

Proton tracks are formed using their hit location in the GEM and RPC walls. We only consider events where the interaction vertex of each proton is reconstructed within the central 26 cm of the target and the distance between them is smaller than 4 cm (Extended Data Fig. 1). The time difference between the RPC and $t_0$ signals define the proton time of flight (TOF) that, combined with the measured track length, is used to determine its momentum.

The protons of interest for the current analysis have momentum between $\sim 1.5$ and 2.5 GeV/c. Thus, events with proton tracks ha ving $\beta > 0.96$ or $< 0.8$ were discarded.

Signals from the TC were combined with the target upstream BCs to form the main $^{12}$C$(p, 2p)$ reaction trigger for the experiment. Additional triggers were set up for monitoring and calibration purposes, see online supplementary materials for details.

Nuclear fragments following the $(p, 2p)$ reaction are emitted at small angles with respect to the incident beam with momentum that is similar to the beam momentum. Three silicon (Si) planes and two MWPCs are placed in the beam-line downstream the target to measure the fragment scattering angle. Following the MWPCs the fragments enter a large acceptance 2.87 T·m dipole magnet. Two drift chambers (DCH) are used to measure the fragment trajectory after the magnet.

The fragment momenta are determined from their measured bending angle in the magnet. Fragment identification (nuclear mass and charge) is done using their bend in the magnetic field and energy deposition in two scintillator BCs placed between the target and the magnet entrance, see Fig. 1b. The latter is proportional to the sum of all fragment charges squared ($Z_{\text{eff}} = \sqrt{\sum Z^2}$).

See Methods and online supplementary materials for additional details on the experimental setup and data calibration procedures.

## SINGLE PROTON KNOCKOUT

We identify exclusive $^{12}$C$(p, 2p)^{11}$B events by requiring the detection of a $^{11}$B fragment in coincidence with two

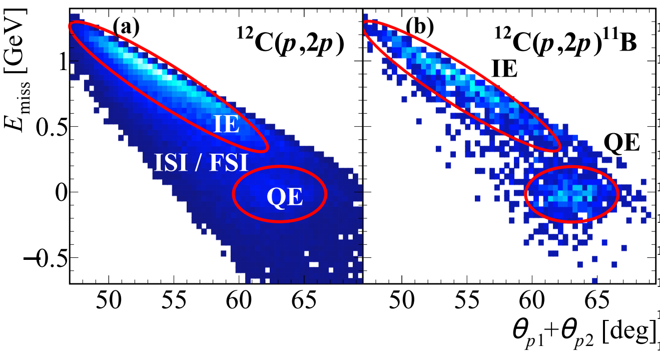


**Fig. 2.** | **Quasi-Free Scattering (QFS) Distributions.** The correlation between the measured missing-energy $E_{\rm miss}$ (Eq. 2) and the two-proton in-plane opening angle for $^{12}(p,2p)$ (a) and $^{12}(p,2p)^{11}B$ (b) events. Quasielastic (QE) events are seen as a peak around low missing energy and opening angles of $\sim 63°$. Inelastic (IE) reactions populate higher missing-energy and lower opening angles while ISI/FSI populate both regions and the ridge between them in the inclusive spectra.

charged particle tracks in the TAS. Energy and momentum conservation for this reaction reads:

$$\bar{p}_{^{12}\rm C} + \bar{p}_{tg} = \bar{p}_1 + \bar{p}_2 + \bar{p}_{^{11}\rm B}, \quad (1)$$

where $\bar{p}_{^{12}\rm C} = (\sqrt{(p^2_{^{12}C} + m^2_{^{12}C})}, 0, 0, p_{^{12}C})$ and $\bar{p}_{tg} = (m_p, 0, 0, 0)$ are respectively the incident beam-ion and target proton four-momentum vectors. $\bar{p}_1$, $\bar{p}_2$, and $\bar{p}_{^{11}\rm B}$ are the four-momentum vectors of the detected protons and $^{11}$B fragment. Assuming QE scattering off a mean-field nucleon we can approximate $\bar{p}_{^{12}\rm C} = \bar{p}_i + \bar{p}_{^{11}\rm B}$, where $\bar{p}_i$ is the initial proton four-momentum inside the $^{12}$C ion. Substituting into Eq. 1 we obtain:

$$\bar{p}_i \approx \bar{p}_{\rm miss} \equiv \bar{p}_1 + \bar{p}_2 - \bar{p}_{tg}, \quad (2)$$

where $\bar{p}_{\rm miss}$ is the measured missing four-momentum of the reaction and is only equal to $\bar{p}_i$ in the case of unperturbed (no ISI/FSI) QE scattering.

Figure 2 shows the measured missing energy ($E_{\rm miss}$, energy component of $\bar{p}_{\rm miss}$) vs. the two-proton in-plane opening angle, $\theta_1 + \theta_2$, for $^{12}{\rm C}(p,2p)$ (left panel) and $^{12}{\rm C}(p,2p)^{11}{\rm B}$ (right panel) events. Both plots show two distinct regions: (A) low missing-energy and large in-plane opening angles that correspond to QE scattering and (B) high missing energy and small in-plane opening angles that correspond to inelastic (IE) scattering.

The inclusive $^{12}{\rm C}(p,2p)$ events are also contaminated by ISI/FSI backgrounds around and underlying both IE and QE regions. This background is not evident in the $^{12}{\rm C}(p,2p)^{11}{\rm B}$ case. This is our first indication that requiring the coincidence detection of $^{11}$B fragments selects a unique subset of one-step processes where a single nucleon was knocked-out without any further interaction with the residual fragment.

To help establish this observation Fig. 3a compares the measured missing-momentum distribution for $^{12}{\rm C}(p,2p)$ QE events with and without $^{11}$B tagging. The QE selection was done using the missing-energy and in-plane opening-angle cuts shown in Fig. 2. From here on all momenta are shown after being boosted to the incident $^{12}$C rest frame. The measured $^{12}{\rm C}(p,2p)$ QE events show a significant high-momentum tail that extends well beyond the nuclear Fermi-momentum ($\approx 250$ MeV/c) and is characteristic for ISI/FSI [2]. This tail is completely suppressed by the $^{11}$B detection.

Figure 3b focuses on $^{12}{\rm C}(p,2p)^{11}{\rm B}$ events and compares the measured $^{11}$B momentum distribution for QE and IE reactions. The fragment momentum distribution is equal for both QE and IE events. This shows that the survival of the fragment selects quasi-free one-step reactions even in the case of inelastic NN scattering and in a kinematical region which is dominated by FSI events.

In unperturbed $^{12}{\rm C}(p,2p)^{11}{\rm B}$ QE scattering reactions the measured missing- and fragment-momenta should balance each other. Fig. 3c shows the distribution of the cosine of the opening angle between the missing- and fragment-momenta. The angle is calculated (only) in the direction transverse to the incident beam-ion as it is not sensitive to boost effects and is thus measured with better resolution. A clear back-to-back correlation is observed, a distinct signature of QE reactions.

$^{12}{\rm C}(p,2p)^{11}{\rm B}$ QE events account for $44.4 \pm 0.6\%$ of the total number of $^{12}{\rm C}(p,2p)$ QE events. We further measured $^{12}{\rm C}(p,2p)^{10}{\rm B}$ and $^{12}{\rm C}(p,2p)^{10}{\rm Be}$ events that correspond to QE scattering to an excited $^{11}$B state that de-excites via neutron or proton emission respectively. These events correspond to $12.2 \pm 2.0\%$ ($^{10}$B) and $\leq 2\%$ ($^{10}$Be) of the total number of $^{12}{\rm C}(p,2p)$ QE events. Therefore, in $\sim 40\%$ of the $^{12}{\rm C}(p,2p)$ QE events the residual nucleus is fragmented to lighter fragments ($Z < 4$). See methods for detailed on the fragment detection efficiency and the systematic uncertainties.

The data shown in Fig. 3 are compared to simulated distributions assuming QE $(p,2p)$ scattering off a $p$-shell nucleon in $^{12}$C. The simulation accounts for the experimental acceptance, and detector resolutions and uses the measured $^1{\rm H}(p,2p)$ elastic scattering cross section and does not include ISI/FSI effects. The total simulated event yield was scaled to match the data. See methods for details.

The simulation agrees well with both missing- and fragment-momentum distributions for QE events and even with the fragment momentum distribution for IE events. This is a clear indication that the requirement to detect a bound $^{11}$B strongly suppresses ISI/FSI and thus provides access to ground-state properties of the measured nuclei. Additional data-simulation comparisons are shown in Extended Data Fig. 2 and 3

The dominance of contributions from secondary reactions to experimentally extracted distributions has been

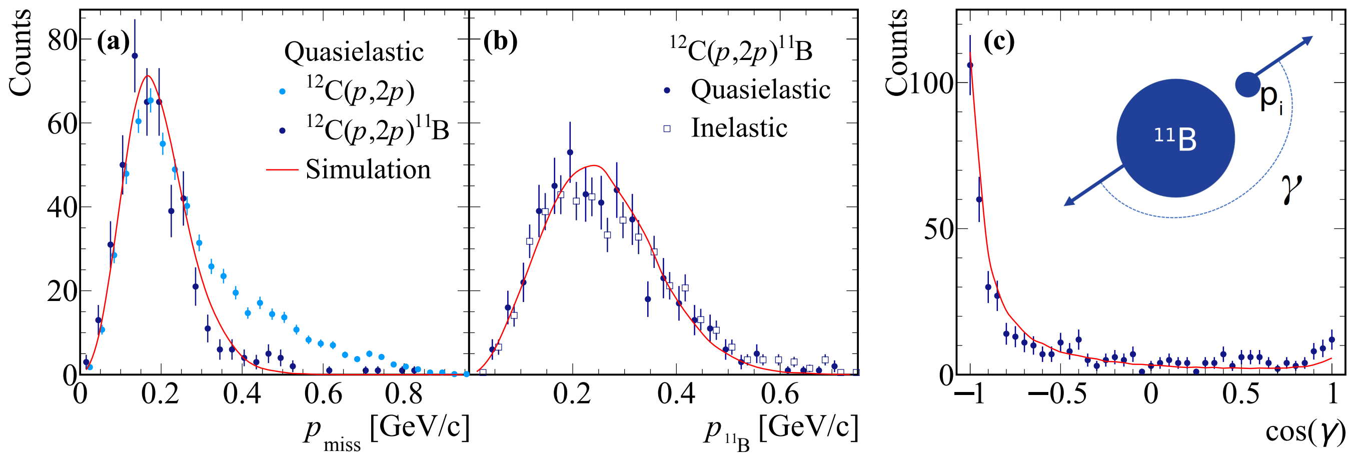


**Fig. 3.** | **Momentum Distributions.** (a) Missing-momentum distribution for quasielastic $^{12}C(p,2p)$ and $^{12}C(p,2p)^{11}B$ events. The distributions are normalized to the peak region. (b) $^{11}B$ fragment momentum distribution for quasielastic and inelastic $^{12}C(p,2p)^{11}B$ events. The light blue points in (a) and the open symbols in (b) have a small artificial offset for better visibility. (c) Distribution of the cosine of the opening-angle between the missing- and fragment-momentum in the plane transverse to the beam. Solid red line shows the result of our quasielastic reaction simulation. Data error bars show statistical uncertainties at the $1\sigma$ confidence level.

a major difficulty in the past even for some reactions using electromagnetic probes. The search for SRC nucleons in electron scattering, for instance, was hampered for several decades by the fact that FSI events stemming from the large-cross section knockout of mean-field nucleons contaminate the high-momentum tail of the extracted nucleon momentum distribution as a background (see Fig. 3a) [8? ? ]. Even in selected kinematical regions in high-resolution experiments, which were able to minimize this contribution [1, 2, 9, 10], the remaining FSI effect had to be taken into account using theoretical estimates. A clear identification of SRC pairs was established only recently by the additional detection of the recoiling partner nucleon [1, 2, 5, 11–14].

At lower beam energies, the method of quasi-free proton-induced nucleon knockout in inverse kinematics has been developed and applied recently to study the single-particle structure of exotic nuclei [15–17]. Here, the data analysis and interpretation relies heavily on the assumption that the extracted particle distributions are free from FSI contamination. Our experiment clearly shows, that ground-state properties of exotic nuclei can be extracted quantitatively by the use of fully exclusive $(p, pN)$ knockout reactions in inverse kinematics at the high-energy radioactive beam facilities.

## HARD BREAKUP OF SRC PAIRS

Next we study SRCs by selecting $^{12}$C$(p, 2p)^{10}$B and $^{12}$C$(p, 2p)^{10}$Be events. The two-proton selection follows the same vertex and $\beta$ cuts mentioned above.

$^{10}$B and $^{10}$Be fragments are produced in SRC breakup events when interacting with a proton-neutron ($pn$) or proton-proton ($pp$) pair, respectively. As $pn$-SRC were shown to be 20 times more abundant than $pp$-SRC pairs [5, 14, 18], we expect to observe 10 times more $^{10}$B fragments than $^{10}$Be. The latter have 2 times larger contribution to the cross-section as the reaction can take place off either proton in the pair.

$^{10}$B and $^{10}$Be fragments can be formed in several ways, as a result of either single-nucleon excitations or two-nucleon correlations. Single-nucleon contributions start with QE single-proton knockout reactions, as discussed above, that result in an excited $^{11}$B fragment that de-excites via neutron emission. In this case the $(p, 2p)$ part of the reaction should be identical to the QE $^{11}$B process, except the $^{10}$B momenta will not correlate with $\mathbf{p}_{\text{miss}}$.

An interaction with a nucleon that is part of an SRC pair will be significantly different. The high relative momentum of nucleons in SRC pairs leads to a large value of $\mathbf{p}_i$ that is largely balanced by a single correlated nucleon, as oppose to the entire $A-1$ nucleons system. Therefore, we require $|\mathbf{p}_{\text{miss}}| > 350$ MeV/c to select SRC breakup events.

IE events where the high-$\mathbf{p}_{\text{miss}}$ is caused by the production of additional particles or by QE interaction followed by FSI that knock out a neutron from the $^{11}$B fragment will not be suppressed by this requirement. IE interactions can be suppressed by requiring a large in-plane opening angle between the protons measured in the $(p, 2p)$ reaction and restricting the missing-energy of the reaction (Fig. 2).

To guide these selections we used the Generalized Contact Formalism (GCF) [3] to simulate $(p, 2p)$ scattering off high missing-momentum SRC pairs. The GCF

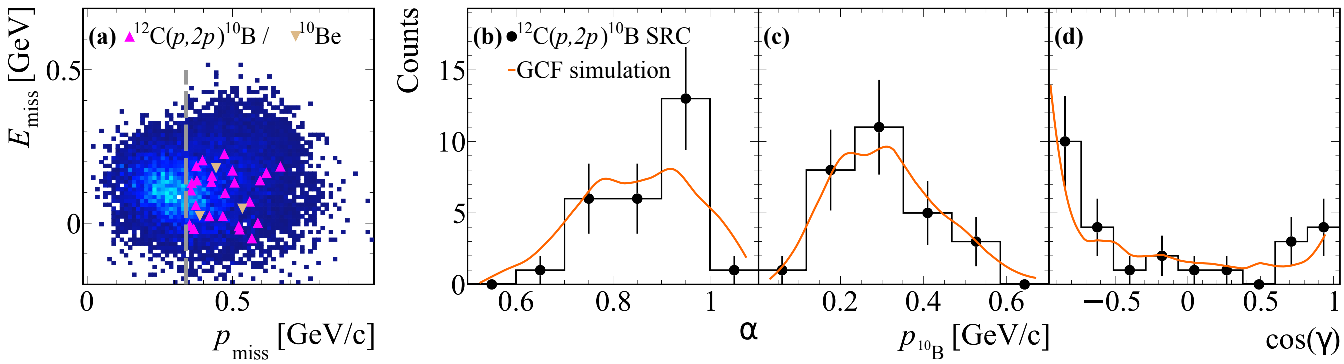


**Fig. 4.** | **Short-Range Correlation Distributions.** (a) Simulated (color scale) and measured (triangles) correlation between the missing-energy and missing-momentum for $^{12}$C$(p,2p)^{10}$B and $^{12}$C$(p,2p)^{10}$Be events. (b) - (d) Measured and simulated distributions of $^{12}$C$(p,2p)^{10}$B events. (b) light-cone momentum distribution, (c) $^{10}$B fragment momentum distribution, (d) distribution of the cosine of the angle between the $^{10}$B fragment and missing-momentum. Solid orange line in (b) - (d) shows the result of our GCF SRC-breakup reaction simulation. Data error bars show statistical uncertainties at the 1$\sigma$ confidence level.

predicts an in-plane opening angle larger than 63° and $-110 \leq E_{\text{miss}} \leq 240$ MeV (see Methods and Extended Data Fig. 4 for details).

Last we use total-energy and momentum conservation to ensure exclusivity by requiring a missing nucleon mass in the entire reaction: $M^2_{\text{miss, excl.}} = (\bar{p}_{^{12}\text{C}} + \bar{p}_{tg} - \bar{p}_1 - \bar{p}_2 - \bar{p}_{^{10}\text{B(Be)}})^2 \approx m_N^2$ (see Extended Data Fig. 5).

We measured 26 $^{12}$C$(p,2p)^{10}$B and 3 $^{12}$C$(p,2p)^{10}$Be events that pass the missing-momentum, missing-energy, in-plane opening angle, and total missing mass cuts described above. These correspond to $<4\%$ of the number of $^{12}$C$(p,2p)$ events passing these SRC selection cuts. Therefore the vast majority of inclusive SRC events result in the formation of light fragments.

If these events were caused by FSI with a neutron in $^{11}$B, we would expect to also detect $^{10}$Be fragments due to FSI with a proton in $^{11}$B. At the high energies of our measurement these two FSI processes have almost the same rescattering cross sections [19]. Our measurement of only 3 $^{10}$Be events is consistent with the SRC $np$-dominance expectation and not with FSI.

Also, as our selection cuts suppress, but do not eliminate, QE scattering events off the tail of the mean-field momentum distribution, some events could result from de-excitation of high-$p_{\text{miss}}$ $^{11}$B fragments. Using the de-excitation cross-sections of Ref. [16] and the measured number of $^{12}$C$(p,2p)^{11}$B events that pass our SRC selection cuts (except for the exclusive missing-mass cut), we estimate a maximal background of 5 $^{10}$B and 2 $^{10}$Be events due to knockout of mean-field protons and subsequent de-excitation.

Figure 4a shows the correlation between the missing momentum and missing energy of the measured $^{10}$B SRC events, compared with their expected correlation based on the GCF simulation. Overall good agreement is observed.

Due to the high momenta of the nucleons in the pair, it is beneficial to analyze the missing-momentum distribution in the relativistic light-cone frame where the longitudinal missing-momentum component is given by $\alpha = (E_{\text{miss}} - p^z_{\text{miss}})/m_p$. $\alpha = 1$ for scattering off standing nucleons. In the $^{12}$C rest frame, $\alpha < 1$ ($> 1$) corresponds to interaction with nucleons that move along (against) the beam direction and therefore decrease (increase) the c.m. energy $s$ of the reaction.

Figure 4b shows the $\alpha$ distribution for the measured SRC events. We observe that $\alpha < 1$, as predicted by the GCF and expected given the strong $s$-dependence of the large-angle elementary proton-proton elastic scattering cross-section.

Next we examine the $^{10}$B fragment momentum distribution in Fig. 4c. For SRC breakup events the fragment is expected to balance the pair c.m. momentum and therefore be consistent with a mean-field momentum distribution given by a three-dimensional Gaussian with width of $\sim 150$ MeV/c [20]. Indeed the fragment follows this distribution, again in agreement with the GCF calculation.

Additional data-simulation comparisons are shown in Extended Data Fig. 6 and 7.

Another important feature of SRC pairs is that they are expected to be scale-separated from the residual nuclear system due to their strong two-body interaction [2, 3]. This predicted factorization implies that there will be no correlation between the pair c.m. and relative momenta. It is assumed in all theoretical models of SRCs, but was never proven experimentally.

Figure 4d shows the distribution of the cosine of the angle between the $^{10}$B fragment momentum and the missing-momentum. The measured distribution shows good agreement with the GCF simulation, that assumes factorization and a lack of angular correlation. This is even more pronounced in comparison with the equivalent distribution for single-nucleon knockout where a strong correlation exists (Fig. 3c) and the strong angular correlation we observe for SRC events between the measured missing-momentum and reconstructed correlated recoil neutron (Extended Data Fig. 7). Therefore by reporting here on the first measurement of SRC pairs with the detection of the residual bound $A-2$ nucleons system we are able to provide first experimental evidence for this aspect of the factorization of SRC pairs from the many-body medium.

## CONCLUSIONS

Our experimental findings clearly demonstrate the feasibility of accessing properties of short-range correlated nucleons in neutron-rich nuclei using high-energy radioactive beams produced at the upcoming accelerator facilities such as FRIB and FAIR. With this method, we accomplished a big step towards realizing the goal of such facilities, which is exploring the formation of visible matter in the universe in the laboratory. Since short-range correlated nucleons are a consequence of density fluctuations in the nucleus, forming locally a high-density environment at zero temperature for a short time, its properties are directly linked to the properties of dense cold nuclear matter.

The experimental method presented here, allows studying the formation and properties of such pairs in a neutron-rich nuclear environment by the use of neutron-rich radioactive nuclear beams. The presented experimental method thus provides a basis to approximate as closely as possible the dense cold neutron-rich matter in neutron stars in the laboratory.


[1] O. Hen, G. A. Miller, E. Piasetzky, and L. B. Weinstein, Rev. Mod. Phys. **89**, 045002 (2017).

[2] C. Ciofi degli Atti, Phys. Rept. **590**, 1 (2015).

[3] R. Cruz-Torres, D. Lonardoni, R. Weiss, N. Barnea, D. W. Higinbotham, E. Piasetzky, A. Schmidt, L. B. Weinstein, R. B. Wiringa, and O. Hen, arXiv (2019), arXiv:1907.03658 [nucl-th].

[4] J. Kelly, Adv. Nucl. Phys. **23**, 75 (1996).

[5] R. Subedi *et al.*, Science **320**, 1476 (2008).

[6] A. Schmidt *et al.* (CLAS Collaboration), Nature **578**, 540–544 (2020).

[7] B. Schmookler *et al.* (CLAS Collaboration), Nature **566**, 354 (2019).

[8] F. Benmokhtar *et al.* (Jefferson Lab Hall A Collaboration), Phys. Rev. Lett. **94**, 082305 (2005).

[9] D. Rohe *et al.* (E97-006 Collaboration), Phys. Rev. Lett. **93**, 182501 (2004).

[10] L. Frankfurt, M. Sargsian, and M. Strikman, International Journal of Modern Physics A **23**, 2991 (2008).

[11] A. Tang *et al.*, Phys. Rev. Lett. **90**, 042301 (2003).

[12] E. Piasetzky, M. Sargsian, L. Frankfurt, M. Strikman, and J. W. Watson, Phys. Rev. Lett. **97**, 162504 (2006).

[13] I. Korover, N. Muangma, O. Hen, *et al.*, Phys. Rev. Lett. **113**, 022501 (2014).

[14] M. Duer *et al.* (CLAS Collaboration), Phys. Rev. Lett. **122**, 172502 (2019), arXiv:1810.05343 [nucl-ex].

[15] T. Kobayashi *et al.*, Nucl. Phys. A **805**, 431c (2008).

[16] V. Panin *et al.*, Phys. Lett. B **753**, 204 (2016).

[17] L. Atar *et al.*, Phys. Rev. Lett. **120**, 052501 (2018).

[18] O. Hen *et al.* (CLAS Collaboration), Science **346**, 614 (2014).

[19] G. Alkhazov, S. Belostotsky, and A. Vorobev, Phys. Rept. **42**, 89 (1978).

[20] E. O. Cohen *et al.* (CLAS Collaboration), Phys. Rev. Lett. **121**, 092501 (2018), arXiv:1805.01981 [nucl-ex].

[21] N. N. A. et al., in *Cryogenics 2019. Proceedings of the 15th IIR International Conference: Prague, Czech Republic, April 8-11, 2019.* (2019).

[22] M. Kapishin (BM@N), Nucl. Phys. A **982**, 967 (2019).

[23] "Conceptual design report bm@n — baryonic matter at nuclotron," ().

[24] S. Khabarov, E. Kulish, V. Lenivenko, A. Makankin, A. Maksymchuk, V. Palichik, M. Patsyuk, S. Vasiliev, A. Vishnevskij, and N. Voytishin, EPJ Web Conf. **201**, 04002 (2019).

[25] Y. Kovalev, M. Kapishin, S. Khabarov, A. Shafronovskaia, O. Tarasov, A. Makankin, N. Zamiatin, and E. Zubarev, Journal of Instrumentation **12**, C07031 (2017).

[26] V. Babkin *et al.*, Nucl. Instrum. Meth. A **824**, 490 (2016).

[27] "Bm@n daq system," ().



**Acknowledgments** add text here.


**Author Contributions** The experimental set up at the Nuclotron was designed and constructed by the BM@N Collaboration at JINR. The design and construction of the TAS was led by G.L. and M.P. Data acquisition, processing and calibration, Monte Carlo simulations of the detector and data analyses were performed by a large number of BM@N Collaboration members, who also discussed and approved the scientific results. The analysis presented here was performed by J.K., M.P., V.L., E.P.S., G.J., V.P., G.L., and M.D., with input from O.H., E.P., T.A., M.K. and A.C., and reviewed by the BM@N collaboration.

**Full Author List**


M. Patsyuk,[1,2] J. Kahlbow,[1,3] M. Duer,[4] V. Lenivenko,[2] E. P. Segarra,[1] G. Johansson,[3] V. Panin,[5,6] G. Laskaris,[1,3] T. Aumann,[4,6,7] A. Corsi,[5] O. Hen,[1] M. Kapishin,[2] E. Piasetzky,[3] Kh. Abraamyan, [2] S. Afanasiev, [2] G. Agakishiev, [2] E. Aleksandrov, [2] I. Aleksandrov, [2] P. Alekseev, [9] K. Alishina, [2] D. Alvear-Terrero,[21] E. Atkin, [11] T. Atovullaev, [2] T. Aushev,[12] V. Babkin,[2] V. Balandin, [2] N. Balashov, [2] A. Baranov, [14] D. Baranov, [2] A. Baranov, [13] N. Baranova, [13] N. Barbashina, [11] P. Batyuk, [2] D. Baznat, [20] M. Baznat, [20] S. Bazylev, [2] A. Beck, [3] D. Blaschke, [21] D. Blau, [10] G. Bogdanova, [13] D. Bogoslovsky, [2] A. Bolozdynya, [11] E.

Boos, [13] K. Boretzky, [6] Y. T. Borzunov, [2] V. Burtsev, [2] M. Buryakov, [2] S. Buzin[2] J. Chen, [16] P. Chudoba, [21] A. Ciszewski, [21] A. Chebotov,[2] B. Dabrowska,[2] D. Dabrowski, [22] D. Dementev, [2] A. Dmitriev, [2] Z. Deng, [17] A. Dryuk, [14] A. Dryablov, [2] P. Dulov,[2] D. Egorov, [2] V. Elsha,[2] A. Fedunin, [2] I. Filippov, [2] K. Filippov, [11] I. Filozova, [2] D. Finogeev,[14] I. Gabdrakhmanov, [2] A. Galavanov, [11] I. Gasparic, [6] O. Gavrischuk, [2] D. Gerasimov, [14] K. Gertsenberger, [2] A. Gillibert, [13] V. Golovatyuk, [2] M. Golubeva, [14] F. Guber,[14] B. Guo,[17] D. Han, [17] Yu. Ivanova, [2] A. Ivashkin, [14] A. Izvestnyy,[14] V. Kabadzhov, [15] S. Kakurin, [2] V. Karjavin, [2] D. Karmanov, [13] N. Karpushkin, [14] G. Kasprowicz, [22] R. Kattabekov, [2] V. Kekelidze, [2] S. Khabarov, [2] P. Kharlamov, [13] A. Khvorostukhin, [20] D. Kirin, [9] Yu. Kiryushin, [2] A. Kisiel, [22] P. Klimai, [12] D. I. Klimanskiy, [2] V. Kolesnikov, [2] A. Kolozhvari, [2] A. V. Konstantinov, [2] Yu. Kopylov, [2] M. Korolev, [13] I. Korover, [3] L. Kovachev, [15] A. Kovalenko, [2] I. Kovalev, [13] Yu. Kovalev, [2] I. Kudryashov, [13] A. Kugler, [18] S. Kuklin, [2] V. Kukulin, [13] E. Kulish, [2] A. Kurganov, [13] S. Kushpil, [18] V. Kushpil, [18] A. Kuznetsov[2] E. Ladygin, [2] D. Lanskoy, [13] I. Larin, [9] N. Lashmanov, [2] M. Ławryńczk, [22] R. Lewandkow, [21] Y. Li, [17] V. Leontiev, [13] M. Linczuk, [22] E. Litvinenko, [2] S. Lobastov, [2] B. Löher,[6] Yu-G. Ma, [16] A. Makankin, [2] A. Makarov, [14] A. Makhnev, [14] A. Maksymchyuk, [2] A. Malakhov, [2] I. Mardor, [3] M. Merkin, [13] S. Merts, [2] H. Miao, [17] V. Mikhailov, [18] A. Morozov, [2] S. Morozov, [14] Yu. Murin, [2] G. Musulmanbekov,[2] R. Nagdasev, [2] S. Nemnyugin, [14] D. Nikitin,[2] D. Oleynik,[2] V. Palchik, [2] A. Petrosyan, [2] Ia. Panasenko, [19] D. Peresunko, [10] M. Peryt, [22] O. Petukhov, [14] Yu. Petukhov, [2] S. Piyadin, [2] S. Plamowski, [22] M. Platonova, [13] V. Plotnikov, [2] J. Pluta, [22] D. Podgainy, [2] G. Pokatashkin, [2] Yu. Potrebenikov, [2] K. Poźniak,[22] A. Reshetin, [14] O. Rogachevsky, [2] V. Rogov, [2] P. Rokita, [22] R. Romaniuk, [22] K. Rosłon, [22] D. Rossi, [4] V. Roudnev, [14] I. Rufanov, [2] P. Rukoyatkin, [2] M. Rumyantsev [2] D. Sakulin, [2] V. Samsonov, [11] H. Scheit, [4] H. R. Schmidt, [19] A. Sedrakian, [21] S. Sedykh, [2] I. Selyuzhenkov, [11] V. Semyachkin, [9] P. Senger, [11] S. Sergeev, [2] C. Shen, [17] A. Sheremetev, [2] A. Sheremeteva, [2] A. Shipunov, [2] M. Shitenkov, [2] M. Shopova, [15] V. Shumikhin, [11] A. Shutov, [2] V. Shutov, [2] H. Simon, [6] I. Slepnev, [2] V. Slepnev, [2] I. Slepov, [2] A. Solomin, [13] A. Sorin, [2] V. Sosnovtsev, [11] V. Spaskov, [2] T. Starecki, [22] A. Stavinskiy, [9] M. Stepanova, [14] E. Streletskaya, [2] O. Streltsova, [2] M. Strikhanov, [11] N. Sukhov, [2] D. Suvarieva,[2] A. Taranenko, [11] N. Tarasov, [2] O. Tarasov, [2] V. Tarasov, [9] A. Terletsky, [2] O. Teryaev, [2] V. Tcholakov, [15] V. Tikhomirov, [2] A. Timoshenko, [2] N. Topilin, [2] B. Topko, [2] H. Törnqvist, [4] T. Traczyk, [22] T. Tretyakova, [13] I. Tyapkin [2] V. Vasendina, [2] A. Vishnevsky, [2] V. Volkov, [13] E. Volkova, [19] A. Voronin, [2] A. Voronin, [13] N. Voytishin, [2] Yi Wang, [17] O. Warmusz, [21] P. Wieczorek, [22] D. Wielanek,[22] Z. Xiao,[17] Z. Xu, [17] I. Yaron, [3] V. Yurevich, [2] W. Zabołotny,[22] N. Zamiatin, [2] M. Zavertiaev, [2] S. Zhang, [16] E. Zherebtsova, [14] N. Zhigareva, [9] X. Zhu, [17] P. Zhuang,[17] A. Zinchenko, [2] Z Zou, [17] E. Zubarev, [2] M. Zuev[2]

[1] Massachusetts Institute of Technology, Cambridge, Massachusetts 02139, USA. [2] Joint Institute for Nuclear Research, Dubna 141980, Russia. [3] School of Physics and Astronomy, Tel Aviv University, Tel Aviv 69978, Israel. [4] Institut für Kernphysik, Technische Universität Darmstadt, 64289 Darmstadt, Germany. [5] IRFU, CEA, Université Paris-Saclay, F-91191 Gif-sur-Yvette, France. [6] GSI Helmholtzzentrum für Schwerionenforschung GmbH, Planckstr. 1, 64291 Darmstadt, Germany. [7] Helmholtz Forschungsakademie Hessen für FAIR, Max-von-Laue-Str. 12, 60438 Frankfurt, Germany. [8] Institute for Nuclear Research of the RAS (INR RAS), Moscow, Russia. [9] Institute for Theoretical and Experimental Physics (ITEP), Moscow, Russia. [10] Kurchatov Institute, Moscow. [11] National Research Nuclear University MEPhI, Moscow, Russia. [12] Moscow Institute of Physics and Technology (MIPT), Moscow, Russia. [13] Skobeltsyn Institute of Nuclear Physics, Moscow State University (SINP MSU), Moscow, Russia. [14] St Petersburg University (SPbU), St Petersburg, Russia. [15] Plovdiv University "Paisii Hilendarski", Plovdiv, Bulgaria. [16] Key Laboratory of Nuclear Physics and Ion-Beam Application (MOE), Institute of Modern Physics, Fudan University, Shanghai, China. [17] Tsinghua University, Beijing, China. [18] Nuclear Physics Institute, CAS, Řež, Czech Republic. [19] University of Tübingen, Tübingen, Germany. [20] Institute of Applied Physics, ASM, Chisinau, Moldova. [21] University of Wroclaw, Wroclaw, Poland. [22] Warsaw University of Technology, Warsaw, Poland.

## Methods

**Ion Beam.** The primary beam ions were produced in a Creon source and accelerated in the Nuclotron [? ]. It had an average intensity of $3 \times 10^5$ ions/sec, delivered quasi-continuously in 3 second long pulses with a 7 second pause between pulses.

The beam contained a mixture of Carbon-12, Nitrogen-14, and Oxygen-16 ions with fractions of 68%, 18%, and 14% respectively. The $^{12}$C ions have a beam momentum of 3.98 GeV/c/u at the center of the $LH_2$ target. The beam ions are identified on an event-by-event basis using their energy loss in the BC detectors (BC1, BC2 in front of the target) that is proportional to their nuclear charge squared $Z^2$. The selection of the incoming nuclear species is shown in Extended Data Fig. 8. Pile-up events are rejected by checking the multiplicity of the BC2 time signal.

**Target upstream detection.** Prior to hitting the target the beam was monitored by two thin scintillator-based beam counters (BC1, BC2) and two multi-wire proportional chambers (MWPCs). The MWPCs determined the incident beam ion trajectory for each event. Besides using the energy deposition in the BCs for particle identification, the BC closer to the target was read-out by a fast MCP-PMT used to define the event start time $t_0$. Beam halo interactions were suppressed using a dedicated BC veto counter (BC-VC), consisting of a scintillator with a 5 cm diameter hole in its center.

**Liquid-hydrogen target.** The target [21] was cryogenically cooled and the hydrogen was recondensated using liquid helium. The liquid hydrogen was held in a 30 cm long and 6 cm diameter aluminized Mylar cylindrical container at 20 Kelvin and 1.1 atmospheres. The container entrance and exit windows were made out of 110 micron thick Mylar.

**Two-arm spectrometer (TAS).** A two-arm spectrometer was placed downstream of the target and was used to detect the two protons from the $(p, 2p)$ reaction that emerge at $24° - 37°$. The vertical acceptance of each arm equals $\pm 18°$. These laboratory scattering angles correspond to 90° QE scattering in the two-protons center-of-mass (c.m). Each spectrometer arm consisted of scintillator trigger counters (TC), gas electron multiplier (GEM) stations, and multi-gap resistive plate chamber (RPC) walls.

Proton tracks are formed using their hit location in the GEM and RPC walls. These allow determining the scattered protons angles relative to the incident beam ion. The vertex resolution along the beam-line direction is 1.8 cm ($1\sigma$) and was measured using a triple-foil lead target as detailed in the Online Supplementary Material.

The time difference between the RPC and $t_0$ signals define the proton time of flight (TOF) that, combined with the measured track length, is used to determine its momentum. Measurements of gamma rays from interactions with a single-foil lead target were used for absolute time-of-flight calibration and determine a resolution of better 100 ps with respect to $t_0$.

Signals from the arm-TC counters were combined with the BC and BC-VC scintillators to form the main $^{12}$C$(p, 2p)$ reaction trigger for the experiment. Additional triggers were set up for monitoring and calibration purposes. More details on the detectors can be found in the Online Supplementary Material.

**Reaction Vertex and Proton Identification.** The $z$-position of the reaction vertex is reconstructed from two tracks in the TAS, while the $(x, y)$ position is obtained from the extrapolated MWPC track in front of the target since this system provides a better position resolution. Details about the algorithm and performance can be found in the Online Supplementary Materials.

The reconstructed vertex position along the beam-line and transverse to it with the liquid-hydrogen target inserted is shown in Extended Data Fig. 1. Clearly, the structure of the target is reconstructed, including the $LH_2$ volume but also scattering from other in-beam materials such as the target walls, styrofoam cover, and various isolation foils. The vertex quality is ensured by requiring that the minimum distance between the two tracks, which define the vertex, is smaller 4 cm. In addition, we place a selection on the absolute $z$-vertex requiring it reconstructs within $\pm 13$ cm from the center of the target.

Scattering at the target vessel that was not rejected by the veto counter is removed by a cut on the $(x, y)$-vertex direction, choosing the strong peak at the entrance of the target (Extended Data Fig. 1).

Having determined the tracks and the vertex, the momenta of the presuming two protons are calculated with respect to the incoming beam direction and using the time-of-flight information between the target and the RPC.

In order to select QFS $(p, 2p)$ events, other particles that also create a track but originating from e. g. inelastic reactions like pions need to be rejected. We apply several criteria, that are further outlined in the next section, but the basic selection is applied to the velocity correlation between the two measured particles which is shown in Supplementary Material Fig. 3a. In the analysis, every particle must pass the velocity condition $0.8 < \beta < 0.96$ that removes fast and slow pions in coincidence with another particle.

**Fragment Detection.** Nuclear fragments following the $(p, 2p)$ reaction are emitted at small angles with respect to the incident beam with momentum that is similar to the beam momentum. Three silicon (Si) planes and two

MWPCs are placed in the beam-line downstream the target to measure the fragment scattering angle. Following the MWPCs the fragments enter a large acceptance 2.87 T·m dipole magnet, and are bent according to their momentum-to-charge ratio ($P/Z$), i. e. magnetic rigidity. Following the magnet, two drift chambers (DCH) with 8 wire-planes each are used to measure the fragment trajectory.

The fragment momenta are determined from the measurement of their bending angle in the magnet. Fragment identification (nuclear mass and charge) is done using their bend in the magnetic field and energy deposition in two scintillator BCs (3,4) placed between the target and the magnet entrance, see Fig. 1b. The latter is proportional to the sum of all fragment charges squared, $Z_{\rm eff} \equiv \sqrt{\sum Z^2}$.

**Fragment Momentum and Identification.** We follow a simulation-based approach to derive $P/Z$ from a multi-dimensional fit (MDF) to the measured fragment trajectories before and after the magnet. The particle trajectory is determined using the MWPC-Si tracking system before the magnet, and using the DCHs after the magnet. Both tracks serve as input for the $P/Z$ determination.

The momentum resolution was determined using empty target measurements of $^{12}$C ions and found to equal 0.7 GeV/c (1.5%) (Supplementary Fig. 2). This resolution is consistent with the resolution expected from our simulation (accounting for the incoming beam energy spread). The achieved momentum accuracy is evaluated to equal 0.2%.

The fragment tracking efficiency, including the detection efficiency of the upstream MWPC-Si, downstream DCH detectors, and track reconstruction algorithm equals $\sim 55\%$. See online Supplementary Materials for details on the tracking algorithms and its performance.

Figure 1 illustrates an example of this fragment identification from the experimental data using $P/Z$ obtained by the MDF vs. total charge measured in the scintillators.

This work focuses only on fragments with nuclear charge of 4 or larger with a single track matched between the upstream and downstream tracks, with or without a proton signal in the TAS. Therefore, although the charge of the fragments is only measured as integrated signal in BC3 and BC4 counters, the Boron isotopes can be selected unambiguously since no possible combination of fragments could otherwise mimic a signal amplitude proportional to $\sum Z^2 = 25$. In the case of $^{10}$Be, the only other fragment of interest here with $Z_{\rm eff} = 4$, contamination from within the resolution is excluded by using the additional $P/Z$ information. $^{10}$Be is the only possible fragment with $P/Z \sim 10$ GeV/c in that region and is well separated.

Besides requesting a good vertex and single global-track events, we employ $Z_{\rm eff}$ and $P/Z$ selection criteria to identify $^{11}$B, $^{10}$B, or $^{10}$Be, namely a two-dimensional charge selection as for the incoming charge but using BC3 and BC4, and additionally a two-dimensional selection in $P/Z$ vs. $Z_{\rm eff}$ as shown in Fig. 1 with a $2\sigma$ selection.

**Single heavy fragment detection efficiencies.** As discussed above, this work is limited to reactions with a single heavy ($Z \geq 4$) fragment in the final state. The detection of such a fragments depends on the ability of the fragment to emerge from the liquid hydrogen target without re-interacting, our ability to identify its charge in the two BCs downstream of the target, and reconstruct its tracks before and after the magnet.

We extract the efficiencies for the charge and track reconstruction using data collected with a beam and no target. We assume that within the quoted uncertainties below, there is no difference between the efficiencies for detecting $Z = 6$ and $Z = 4$ and 5 fragments.

The charge determination efficiency in the BSs downstream the target was determined by selecting incident $^{12}$C ions based on their energy loss in the BC1 and BC2 counters (see Extended Data Fig 8). We then examine the fraction of those $^{12}$C ions also identified by their energy loss in BC3 and BC4 downstream the target. This fraction defines a charge identification efficiency of $\epsilon_z = 83 \pm 6\%$, where the uncertainty is obtained from examining different energy-deposition cuts of $2 - 5\sigma$. The fraction of such $Z_{in} = Z_{out} = 6$ events with a single reconstructed track and $P/Z = 8$ GeV/c is equal to $50 \pm 5\%$.

When the liquid-hydrogen target is in place, fragments are attenuated due to their interaction in the target after the fundamental $^{12}$C-p interaction. We estimate this lose assuming an effective target density of $\rho = 2$ g/cm$^2$ and a total reaction cross section of $\sigma_{tot} = 220 \pm 10$ mb. The overall flux reduction was estimate to equal $att = exp(-\rho\sigma_{tot}) = 0.75 \pm 0.01$ and was corrected for in the data analysis.

**Single-Proton Knockout Data-Analysis.** The basic selection criteria for any analysis require an incoming $^{12}$C, as well as a good reaction vertex, while the particles in the arms pass the velocity condition. That is called the inclusive $(p, 2p)$ reaction channel which is dominated by FSI and IE scattering. The exclusive reaction channel requires the additional detection of a $^{11}$B fragment, with a single global-track condition and defines the one-proton Quasi-Free Scattering (QFS), still being contaminated by IE scattering.

We select explicitly bound states in $^{11}$B where the $3/2^-$ ground-state is populated with the largest cross section while bound excited states that de-excite via $\gamma$-ray emission cannot be distinguished. However, those excited states are also populated in a $p$-shell knockout, but only with a small cross section as found in a previous study [16]. The only two significant $1/2^-$ and $3/2^-$ states contribute with 10% and 8% percent to the total cross sections, respectively. In order to identify real $(p, 2p)$ QE events and reject IE events, we chose missing energy and the in-plane opening angle of the two particles measured in the arms, looking at quantities that are reconstructed from that independent detection system.

The missing energy is defined as $E_{\text{miss}} = m_p - e_{\text{miss}}$, where $e_{\text{miss}}$ is the energy component of $\bar{p}_{\text{miss}}$ in the rest frame of the $^{12}$C nucleus. The boost from the laboratory system into the rest frame is applied along the incoming-beam direction considering the reduced beam energy at the reaction vertex. The selection region for QE events is defined in the exclusive channel with fragment selection, in a $2\sigma$ ellipse as indicated in Fig. 2. The IE part is defined from the remaining events within the other ellipse. The same criteria are applied in the inclusive channel. Correlations in other kinematical variables are shown in Extended Data Fig. 9.

The $M^2_{\text{miss}}$ spectrum in Extended Data Fig. 2a shows the squared missing mass for the exclusive channel before and after applying the QE cut, clearly showing that we select background-free QE events from around the proton mass. A lower boundary in the squared missing mass of $M^2_{\text{miss}} > 0.47$ GeV$^2/c^4$ is only applied for sanity. While we are aware of the fact that the chosen selection criteria might influence other kinematical variables of $\bar{p}_{\text{miss}}$, we show the momentum distributions and angular correlations with less strict selection in the Extended Data (Figs. 2, 3) which do not show a different behavior and are also described well by the simulation.

**Single-Proton Knockout Simulation.** We compare the QFS-elastic $^{12}$C$(p, 2p^{11}$B) data to a MonteCarlo simulation for the proton quasielastic scattering off a moving $^{12}$C. In the calculation, the $^{12}$C system is treated as spectator plus initial proton, $\mathbf{p}_{^{12}\text{C}} = \mathbf{p}_{^{11}\text{B}} + \mathbf{p}_i$. The proton's initial momentum distribution in $^{12}$C is sampled from a theoretical distribution that is calculated from a Woods-Saxon potential for $p_{3/2}$ proton with binding energy of $S_p = 15.96$ MeV, not including absorption effects [? ].

We raffle $|\mathbf{p}_i|$ from the total-momentum distribution and randomize its direction. The proton's off-shell mass is

$$m^2_{\text{off}} = m^2_{^{12}\text{C}} + m^2_{^{11}\text{B}} - 2m_{^{12}\text{C}} \cdot \sqrt{m^2_{^{11}\text{B}} + \mathbf{p}^2_i}. \quad (3)$$

The two-body scattering between the proton in $^{12}$C and the target proton is examined in their c.m. frame. The elastic-scattering cross section is parameterized from free $pp$ differential cross section data. Following the scattering process, the two protons and $^{11}$B four-momenta are boosted back into the laboratory frame.

The two-arm spectrometer was placed such that it covers the symmetric, large-momentum transfer, 90° c.m. scattering region. Given the large forward momentum, the detectors cover an angular acceptance of $\sim 24° < \theta < 37°$ in the laboratory system which corresponds to $\sim 74° < \theta_{\text{c.m.}} < 104°$ in the c.m. frame.

In order to compare the simulated data to the experimental distributions, the simulation is treated and analyzed in the same way as the experimental data. Experimental acceptances are included. Resolution effects are convoluted to proton and fragment momenta. The proton time-of-flight resolution is 0.9% and the angular resolution 5 mrad, while the fragment momentum resolution is 1.5% and the angular resolution 1.1 mrad in $x$ and $y$. The angular resolution of the incoming beam is 1.1 mrad. The beam-momentum uncertainty, examined as Gaussian profile, does not significantly impact rest-frame momentum distribution as long as the nominal beam momentum is the same used for experimental data and the simulated ion. However, the momentum distributions are dominated by the width of the input distribution. When comparing, the simulation is normalized to the integral of the experimental distributions. We find overall good agreement between experiment and MonteCarlo simulation showing that the reaction mechanism and QE events sample the proton's initial momentum distribution inside $^{12}$C. Additional data-simulation comparison are shown in Extended Data Fig. 3.

**Selecting high-momentum SRC events.** We study SRC events by focusing on $^{12}$C$(p, 2p)^{10}$B and $^{12}$C$(p, 2p)^{10}$Be events. We start with the two-proton detection following the vertex and $\beta$ cuts mentioned above. The first cut applied to select SRC breakup events is to look at high-missing momentum, $p_{\text{miss}} > 350$ MeV/c.

The remaining event selection cuts are chosen following a GCF simulation of the $^{12}$C$(p, 2p)$ scattering reaction off high missing-momentum SRC pairs. After applying the high-missing momentum cut, we look at the in-plane opening angle between the protons for different cases: (a) inclusive $^{12}$C$(p, 2p)$ events, (b) GCF simulated events, (c) exclusive $^{12}$C$(p, 2p)^{10}$B events, and (d) $^{12}$C$(p, 2p)^{10}$Be events. The GCF predicts relatively large opening angles that guides our selection of in-plane opening angle larger than 63° (that also suppresses contributions from inelastic reactions that contribute mainly at low in-plane angles).

Next we apply a missing-energy cut to further exclude inelastic and FSI contributions that appear at very large missing-energies. To this end we examine the correlation between the missing energy and missing momentum, after applying the in-plane opening angle cut, for the full range of the missing momentum (i.e., without the $p_{\text{miss}} > 350$ GeV/c cut), see Extended Data Fig. 4. We chose to cut on $-110 < E_{\text{miss}} < 240$ MeV.

To optimize the selection cuts we use the total energy and momentum conservation in reactions at which we identified a fragment ($^{10}$B or $^{10}$Be). We can write the exclusive missing-momentum in these reactions as

$$\bar{p}_{\text{miss,excl.}} = \bar{p}_{^{12}\text{C}} + \bar{p}_{tg} - \bar{p}_1 - \bar{p}_2 - \bar{p}_{^{10}\text{B(Be)}}. \qquad (4)$$

Neglecting the center-of-mass motion of the SRC pair, the missing-mass of this 4-vector should be equal to the nucleon mass $m^2_{\text{miss,excl.}} \backsimeq m^2_N$. The distributions for $^{12}\text{C}(p,2p)^{10}\text{B}$ and $^{12}\text{C}(p,2p)^{10}\text{Be}$ events that pass the missing-momentum, in-plane opening angle, and missing-energy cuts are shown in Extended Data Fig. 5 together with the GCF simulation. To avoid background events with very small values of the missing-mass we choose to cut on $M^2_{\text{miss,excl.}} > 420$ MeV$^2$/c$^4$. After applying this cut we are left with 26 $^{12}\text{C}(p,2p)^{10}\text{B}$ and 3 $^{12}\text{C}(p,2p)^{10}\text{Be}$ events that pass all the SRC cuts.

**Characterizing the selected $^{12}\text{C}(p,2p)^{10}\text{B}$ events.** The majority of SRC events with a detected fragment comes with $^{10}$B. In the Extended Data we present some kinematical distributions of these selected events together with the GCF simulation. Extended Data Fig. 6 shows the total missing-momentum as well as its different components, and also the same for momentum of the $^{10}$B fragment, which is equivalent for the center-of-mass motion of the SRC pair. Overall good agreement between the data and simulation is observed.

For $^{10}$B, if the scattering was done off an $np$ SRC pair, then the exclusive missing-momentum we defined in Eq. 4 should be equal to the initial momentum of the undetected neutron $\bar{p}_{\text{miss,excl.}} \backsimeq \bar{p}_n$. Assuming that the missing momentum $\bar{p}_{\text{miss}}$ is the initial momentum of the proton inside the carbon nucleus, then for an $np$ SRC pair with large relative momentum and small center-of-mass momentum for the two nucleons, the opening angle between their vector should show a clear back-to-back correlation, i.e., 180 degrees. This angular distribution is shown in Extended Data Fig. 7, for the total opening angle and the one in the transverse direction. A strong peak can be observed in both distributions, especially in the transverse distribution due to its better resolution. The 1D distribution for the missing energy is shown in Extended Data Fig. 7c.

933

# Extended Data

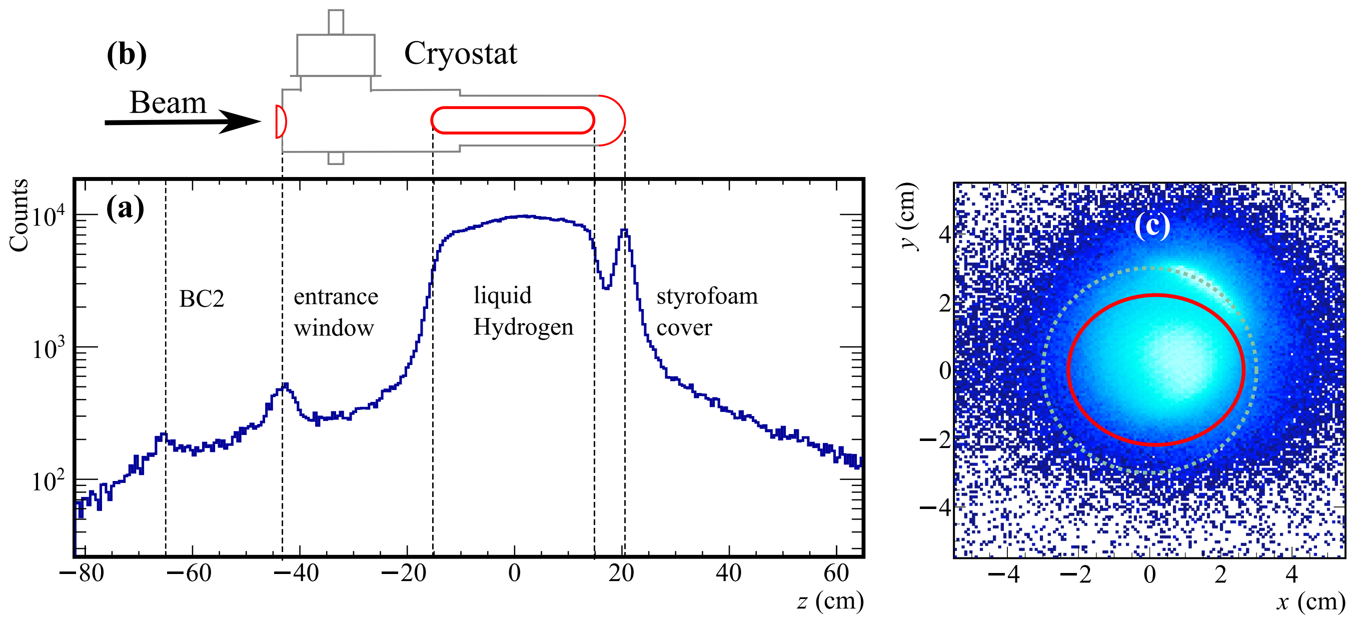


**Extended Data Fig. 1.** | **Reaction Vertex.** Reconstructed reaction vertex in the $LH_2$ target. The position along the beam line is shown in (a), scattering off in-beam material is also visible. For comparison, a sketch of the target device is shown in (b), scattering reactions are matched at the entrance window, the target vessel, styrofoam cover. A selection in $z < |13\text{ cm}|$ is applied to reject such reactions. The $xy$ position at the reaction vertex is shown in (b), measured with the MWPCs in front of the target. The dashed line indicates the target cross section. Scattering at the target vessel at around ($x = 2\,\text{cm}$,$y = 2\,cm$) can be seen which is removed by the selection as indicated by the red circle.

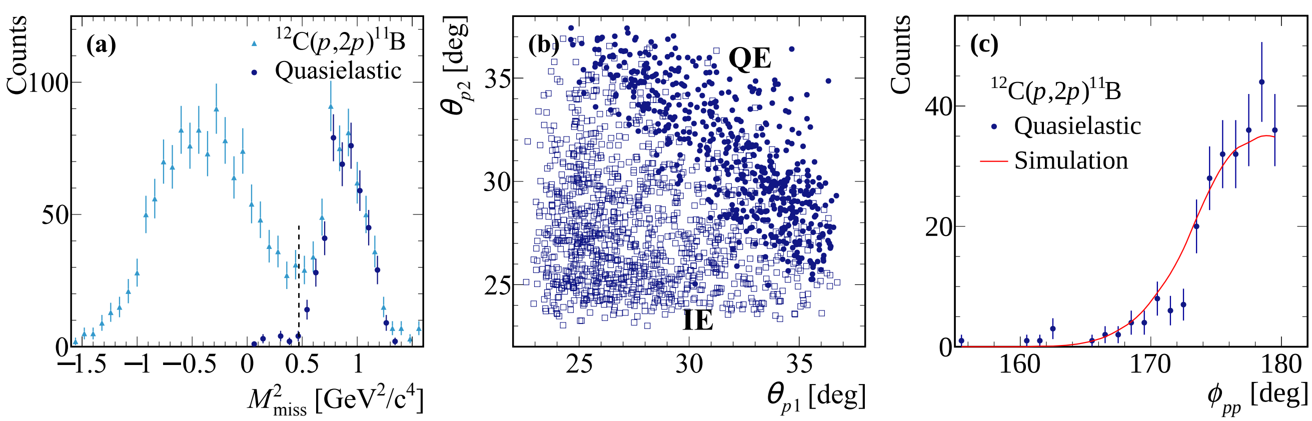


**Extended Data Fig. 2.** | **Proton-proton Correlations.** (a) Proton missing mass for $^{12}\mathrm{C}(p, 2p)^{11}\mathrm{B}$. After the QE selection in $E_{\text{miss}}$ and in-plane opening angle, the distribution is shown in dark blue dots with artificial offset for better visibility. We apply an additional missing mass cut $M^2_{\text{miss}} > 0.47$ GeV$^2$/c$^4$, indicated by the dashed line. (b) Angular correlation between the two $(p, 2p)$ protons for quasielastic ($M^2_{\text{miss}} > 0.55$ GeV$^2$/c$^4$) and inelastic ($M^2_{\text{miss}} < 0.55$ GeV$^2$/c$^4$) reactions only selected by missing mass. The QE events show a strong correlation with a polar opening angle of $\sim 63^\circ$. (c) The off-plane opening angle for $M^2_{\text{miss}} > 0.55$ GeV$^2$/c$^4$ peaks at 180° as expected. Notice that our experiment has a limited acceptance.

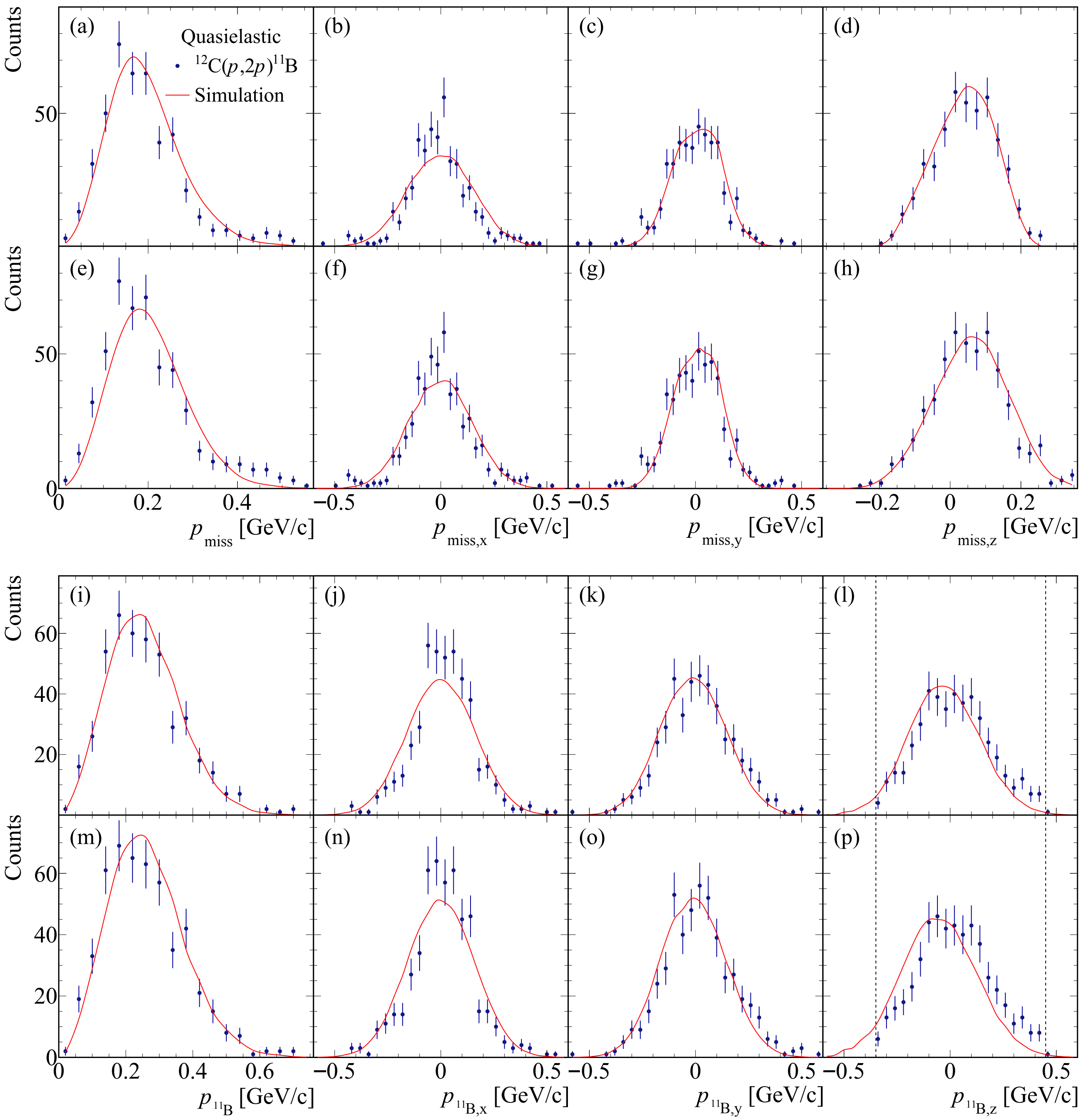


**Extended Data Fig. 3.** | **Missing and Fragment Momentum.** Momentum components for quasielastic $^{12}$C$(p, 2p)^{11}$B reactions compared to simulation. The proton missing momentum is shown for (a)-(d), while (e)-(h) show the same distributions but with missing mass cut only (0.55 GeV$^2$/c$^4$ < $M^2_{\rm miss}$ <1.40 GeV$^2$/c$^4$). Agreement with the simulation is found in both cases. The shift in $p_{{\rm miss},z}$ is associated with a strong $pp$ cross-section scaling with c.m. energy. For the same conditions the $^{11}$B fragment momentum components are shown in (i)-(l), and (m)-(p). The dashed lines in $p_{^{11}{\rm B},z}$ indicate the momentum acceptance due to the fragment selection in $P/Z$.

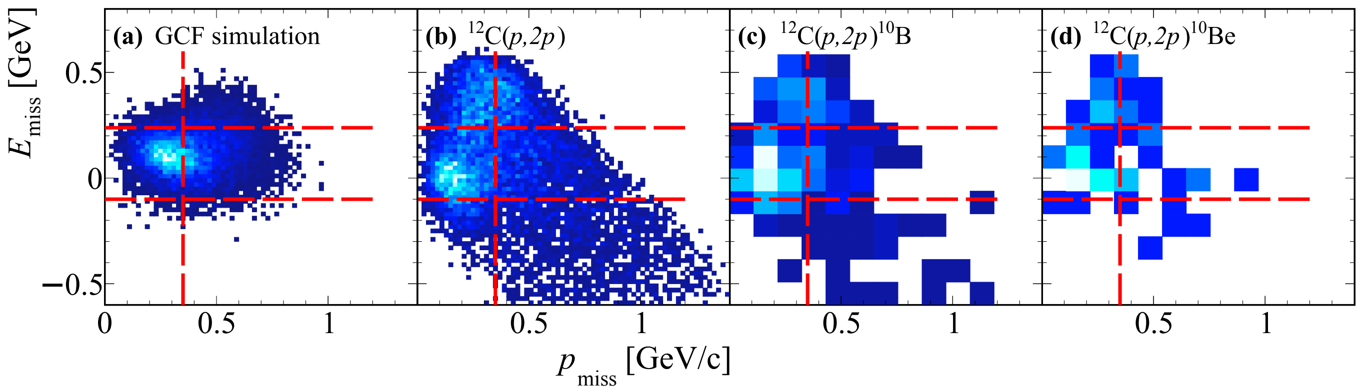


**Extended Data Fig. 4.** | **SRC Selection.** The missing energy vs. missing momentum for (a) GCF simulation, (b) $^{12}$C$(p,2p)$, (c) $^{12}$C$(p,2p)^{10}$B, and (d) $^{12}$C$(p,2p)^{10}$Be events that pass the in-plane opening angle cut. The selection cuts in $-110$ MeV$< E_{\rm miss} < 240$ MeV and $p_{\rm miss} > 350$ MeV/c are indicated by the dashed lines.

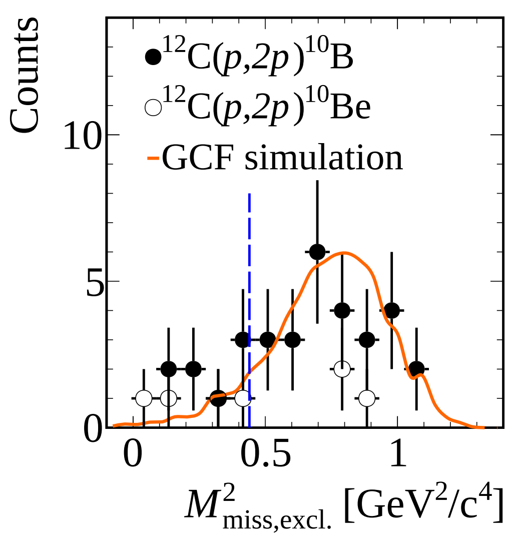


**Extended Data Fig. 5.** | **SRC Missing Mass.** The exclusive missing mass distributions for $^{12}$C$(p,2p)^{10}$B events and $^{12}$C$(p,2p)^{10}$Be events that pass the missing momentum, in-plane opening angle, and missing energy cuts together with the GCF simulation (orange). The blue line represents the applied cut on the exclusive missing-mass $M^2_{\rm miss,excl.} > 0.42$ GeV$^2$/c$^4$.

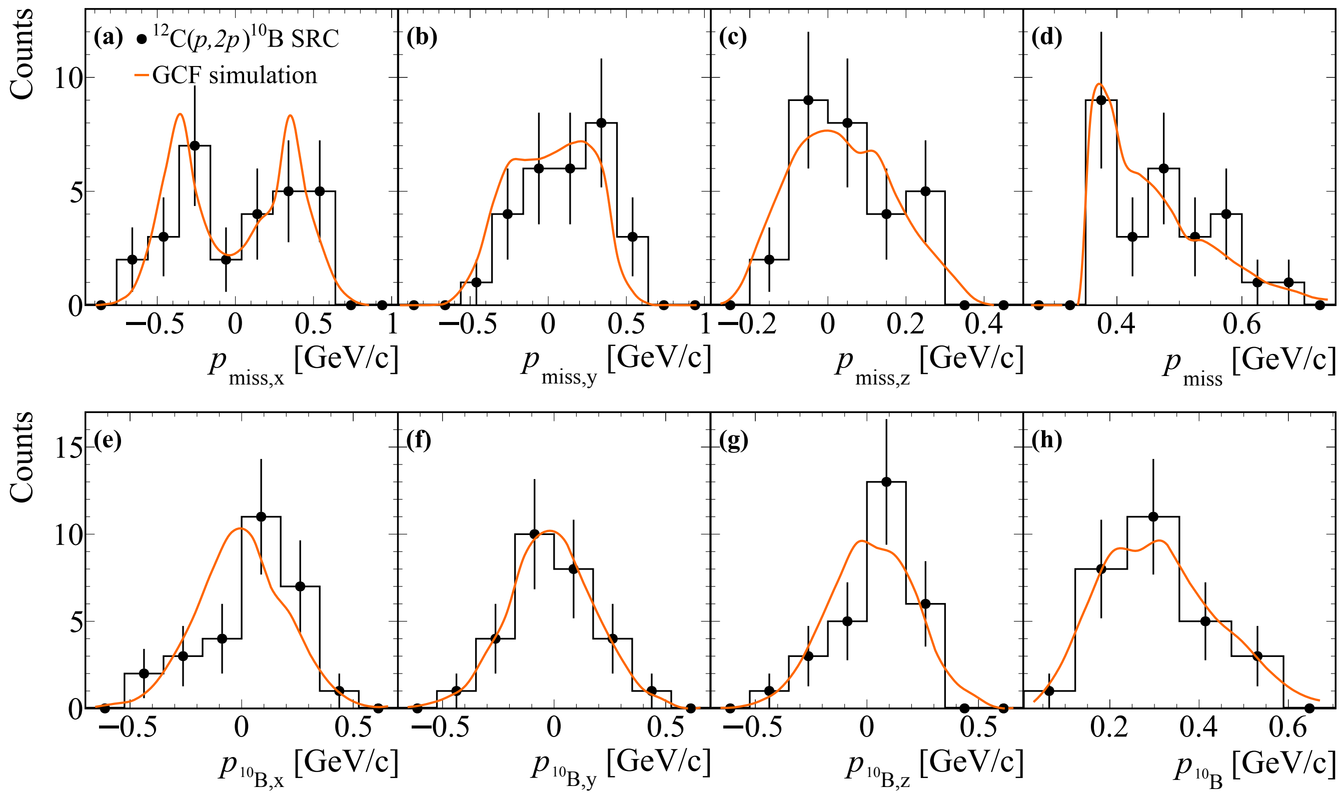


**Extended Data Fig. 6.** | **SRC Missing and Fragment Momentum.** The missing momentum distributions (a)–(d) for the selected $^{12}$C$(p,2p)^{10}$B SRC events (black) together with the GCF simulation (orange). Acceptance effects, especially in the transverse direction are well captured by the simulation. The lower figures (e)–(h) show the fragment momentum distributions in the rest frame of the nucleus for the same selected $^{12}$C$(p,2p)^{10}$B SRC events (black) together with the GCF simulation (orange).

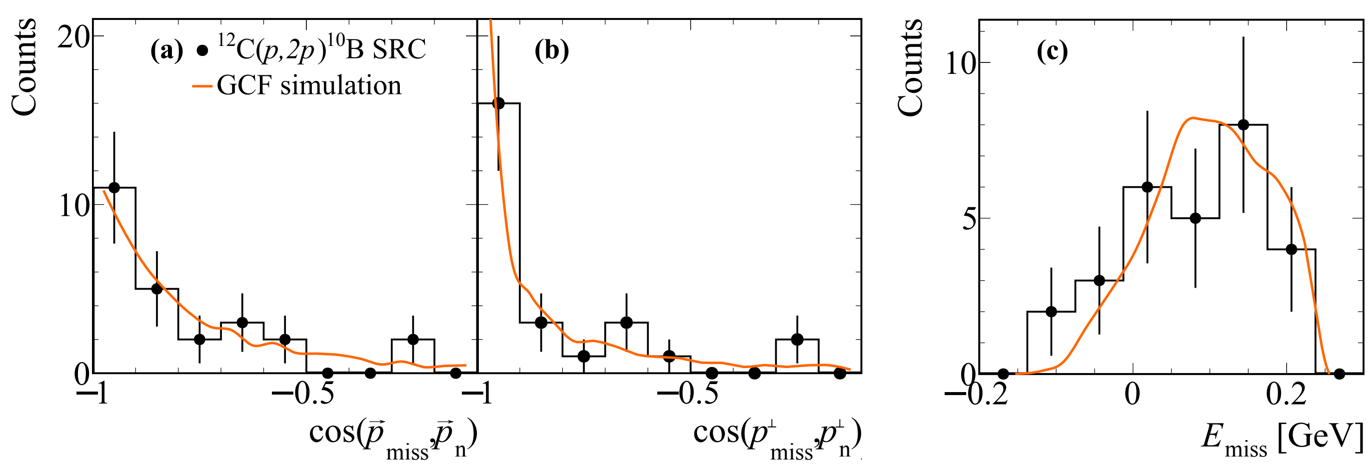


**Extended Data Fig. 7.** | **SRC Opening Angle.** (a) Opening angle between the missing momentum and the neutron reconstructed momentum for the selected $^{12}$C$(p,2p)^{10}$B SRC events (black) together with the GCF simulation (orange). (b) The transverse opening angle. (c) Missing energy distribution for the selected $^{12}$C$(p,2p)^{10}$B SRC events (black) together with the GCF simulation (orange).

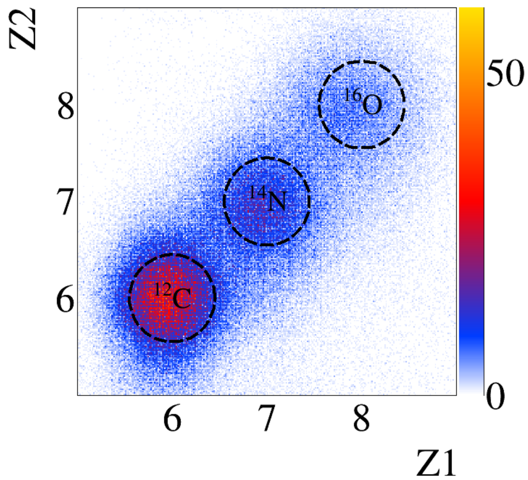


**Extended Data Fig. 8.** | **Incoming Beam Ions.** Charge identification of incoming beam ions measured event-wise using the two BC counters in front of the target (BC1, BC2). Besides $^{12}$C, the $A/Z = 2$ nuclei $^{14}$N and $^{16}$O are mixed in the beam with less intensity.

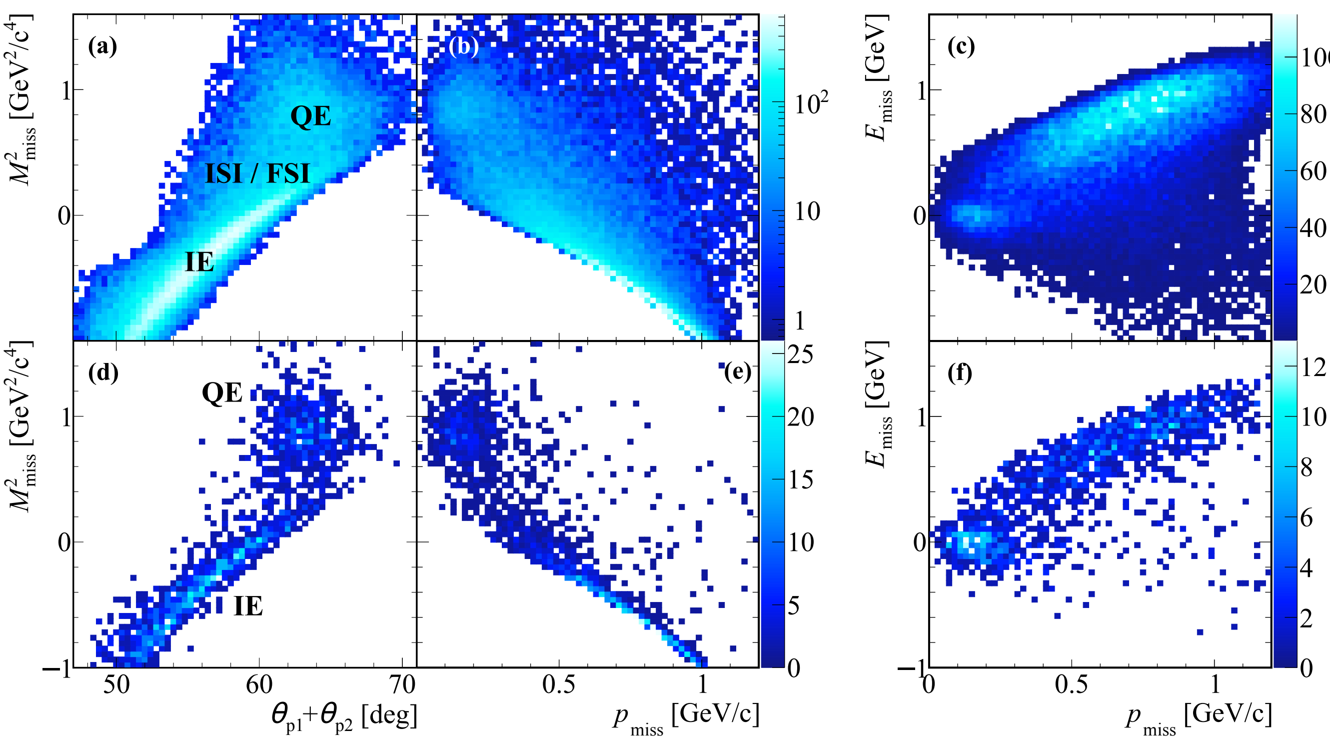


**Extended Data Fig. 9.** | **Kinematical Correlations in single-proton Knockout.** Figures (a)-(c) show the inclusive $^{12}$C$(p, 2p)$ channel, and (d)-(f) the exclusive channel, i.e. with tagging $^{11}$B. In both cases, the quasielastic peak (QE) and inelastic (IE) events are visible, while ISI/FSI are reduced by the fragment tagging. Eventually, a selection in $E_{\text{miss}}$ and in-plane opening angle was chosen to select QE events, see Fig. 2. The distributions are not corrected for fragment-identification efficiency.

# Supplementary Materials for: Unperturbed inverse kinematics nucleon knockout measurements with a 48 GeV/c Carbon beam

**1. BM@N Detector Configuration.** The BM@N experimental setup at JINR allows to perform fixed-target experiments with high-energy nuclear beams that are provided by the Nuclotron accelerator [22]. Our experiment was designed such that in particular protons under large laboratory angles can be measured. That dictated a dedicated upstream target position and modified setup as used for studies of baryonic matter, but using the same detectors [23]. The setup comprises a variety of detection systems to measure positions, times, and energy losses to eventually obtain particle identification and determine their momenta. We are using scintillator detectors, multi-wire proportional chambers, Silicon strip detectors, drift chambers, gas-electron multipliers, and resistive plate chambers as shown in Fig. 1 and described in the following.

Beam Counters (BC): A set of scintillator counters, installed in the beam-line, based on a scintillator plate with an air light guide read in by a PMT were used. Two counters (BC1 and BC2) were located before the target: BC1 was located at the beam entrance to the experimental area. It is a 15 cm in diameter and 3 mm thick scintillator read out by a XP2020 Hamamatsu PMT. BC2 was located right in front of the target and provided the start time $t_0$. This scintillator is of 4 cm x 6 cm x 0.091 cm size, and was tilted by 45° so that its effective area was around 4 cm x 4 cm. It was read out by a Photonis MCP-PMT PP03656. Two counters (BC3 and BC4), each read out by a XP2020 PMT, were located downstream the target to measure the total charge of the fragment particles in each event. BC3 was based on 10 cm x 10 cm x 0.29 cm scintillator, and the BC4 was 7 cm x 7 cm x 0.3 cm. A veto-counter with the dimensions of 15 cm x 15 cm x 0.3 cm and a hole of 5 cm in diameter was located between BC2 and the target. It was read out by an XP2020 PMT and was included in the reaction trigger to suppress the beam halo.

Multi-wire proportional chambers (MWPC): We used two pairs of MWPC chambers, one before and one after the target for in-beam tracking [24]. Each chamber has six planes X, U, V, X', U', V'. The X wires are aligned in $y$ direction, U and V planes are oriented ±60° to X. The distance between wires within one plane is 2.5 mm, the distance between neighboring planes is 1 cm. In total 2304 wires are read out. The active area of each chamber is 500 cm$^2$ (22 cm x 22 cm). About 1 m separated the chambers in the first pair upstream the target and 1.5 m between the chambers in the second pair downstream the target. The polar angle acceptance of the chambers downstream the target is 1.46°. The efficiency of the MWPC pair in front of the target for particles with the charge of 6 is (92.2±0.1)%. The efficiency of the MWPC pair after the target is (88.8±0.7)% for ions with $Z = 6$, and (89.1±0.2)% for ions with $Z = 5$.

Silicon trackers (Si): As additional tracking system, three Silicon planes [25] were located after the target. In combination with the MWPCs after the target, an increased tracking efficiency is reached. The first and second Si planes share the same housing. The first plane consists of four modules, the second plane has two modules, the third plane has eight modules. Each module has 640 $X$-strips (vertical) and 640 $X'$-strips (tilted 2.5° relative to $X$ strips). The first plane has smaller modules with 614 $X'$ strips and 640 $X$ strips. The first two planes and the third plane are separated by 109 cm. The angular acceptance of the Si detector system is 1.58°. The design resolution of 1 mm for the $y$-coordinate and 50 $\mu$m for the $x$-coordinate was achieved in the experiment. The efficiency and acceptance of the Si tracking system, determined for reconstructed MWPC tracks before the target, is $(89.1 \pm 0.8)$% for outgoing $Z = 6$ ions, and $(88.8 \pm 0.7)$% for $Z = 5$ isotopes.

Combined tracks were reconstructed using information from the MWPC pair after the target and the Si detectors. The efficiency to find a Si track or a track in the second pair of the MWPC or a combined track, evaluated for events with reconstructed the track before the target, is $(97.7 \pm 0.2)$% for $Z = 6$ ions, and $(97.9 \pm 0.3)$% for $Z = 5$ isotopes.

Drift Chambers (DCH): Two large-area drift chambers, separated by 2 m, are located downstream the bending magnet. These detectors are used for tracking the charged fragments in the forward direction. Together with the upstream-tracking information of MWPC and Si in front of the magnet, the bending angle and thus the magnetic rigidity of the ions is determined. Each chamber consists of eight coordinate planes: X, Y, U, V, where X wires are parallel to the $x$-axis, Y wires are at 90° relative to X, and U and V are tilted by $+/-45°$, respectively. The distance between wires within one plane is 1 cm, in total 12,300 wires are read out. The spatial resolution, given as residual resolution, for one plane (X, Y, U, or V) is around 200 $\mu$m ($1\sigma$). It is obtained by the difference between the measured hit and the position from the reconstructed track at that plane. The efficiency of around 98% (97%) for each plane was estimated for the first (second) DCH based on the reconstructed matched track in the second (first) DCH. A reconstructed track within one DCH chamber has at least 6 points.

Two-Arm Spectrometer (TAS): In order to detect light charged particles from the target, scattered to large laboratory angles, the symmetric two-arm detection system around the beamline was constructed for this experiment. Each arm, placed horizontally at $+/-29.5°$ (center) with respect to the beamline, was configured by the following detectors along a 5 m flight length: scintillator – scintillator – GEM – RPC. Each arm holds one GEM (Gas-Electron

Multiplier) station at a distance of 2.3 m from the target. Each GEM station contained two GEM planes with the dimensions of 66 cm ($x$) x 40 cm ($y$) each, placed on top of each other (centered at $y = 0$) to increase the overall sensitive area to 66 cm x 80 cm. The spatial resolution of the GEM hit is 300 $\mu$m. Each RPC detector station, located at the end of the two arms at a distance of 5 m from the target, has a sensitive area of 1.1 m x 1.2 m. Each station consists of two gas boxes next to each other, each holds 5 multi-gap Resistive-Plate Chambers (RPCs) planes inside [26]. Two neighboring planes within one box overlap by 5 cm in $y$ direction. Each plane has 30 cm long 1.2 cm wide horizontally aligned readout strips with a pitch of 1.25 cm. The measured $x$ position is obtained by the time difference measured between the ends of one strip. The resolution is 0.6 cm. Together with the position information from the GEM, tracks are reconstructed along the arms and the time-of-flight information is taken from the RPC system. The clustering algorithm was applied to the neighboring strips fired in the same event. In addition, each arm was equipped with two trigger counters (TC), scintillator planes close to the target. The X planes consisted of two scintillators with dimensions of 30 cm x 15 cm x 0.5 cm located horizontally side by side and read out by a Hamamatsu 7724 PMT each. The distance between the target center and the X-counters was 42 cm. Each Y plane was a single scintillator piece of 50 cm x 50 cm x 2 cm, read out by two ET9954KB PMTs. The distance between the target center and the Y planes was 170 cm. Each arm covers a solid angle of 0.06 sr, limited by the RPC acceptance.

Data Acquisition System (DAQ) and Triggers: The DAQ performs readout of the front-end electronics of the BM@N detectors event-by-event based on the information of the trigger system [27]. Timing information were read out from DCH and RPC (two-edge time stamp) and processed by Time to Digital Converters (TDC) based on HPTDC chip with typical accuracy of 20 ps for RPC and 60 ps for DCH. The amplitude information were read out from coordinate detector systems of Si and GEMs and processed by Amplitude to Digital Converters (ADC). The last 30 $\mu$s of waveforms were read back. The clock and time synchronization was performed using White Rabbit protocol. As mentioned in the main text, the reaction trigger was set up requesting an incoming and outgoing ion in coincidence with signals in the left and right arm trigger scintillator-counters (TC). Additional triggers are built from coincident signals in the various scintillator detectors, suited for either calibration purposes or data taking. The trigger matrix is shown in Table I, creating the so-called Beam trigger, Interaction trigger, and the physics triggers AndSRC, and OrSRC. The input signals are BC1, BC2, no veto signal (!BC-VC), and a signal in BC3 which does not exceed a certain upper threshold (!hBC3). The coincidence condition AndXY requires signals in all TCs in the left and right arm, while OrXY takes the OR between the left and right arm of the spectrometer. The phyiscs data were taken requesting the AndSRC trigger at a rate of about 100 Hz, allowing a livetime of close to 100%.

**Supplementary Table I.** | **Trigger Matrix.** Different coincidence triggers for collecting the data.

| Trigger | BC1 | BC2 | !BC-VC | !hBC3 | AndXY | OrXY |
|---|---|---|---|---|---|---|
| Beam | x | x | x | | | |
| Interaction | x | x | x | x | | |
| AndSRC | x | x | x | x | x | |
| OrSRC | x | x | x | x | | x |

**2. Fragment Momentum Calculation** Charged particles are bent in the large analyzer magnet in the orthogonal magnetic field according to their magnetic rigidity, i. e. momentum-over-charge ratio $B\rho = P/Q$. And thus allows to determine the fragment total momenta.

For this purpose, simulations of the fragments, propagating in the magnetic field, were carried out using the standard field map of the magnet. The corresponding materials of the beam-line detectors were also implemented in the simulation. The simulated fragments were chosen to have the maximum possible position, angular and momentum spread to cover the entire geometrical acceptance of the magnet and detectors. The output of the simulation is used afterwards as a training sample for the multidimensional fit (MDF) algorithm (https://root.cern.ch/doc/master/classTMultiDimFit.html) in the form of n-tuples which hold positions and angles of the fragment trajectory upstream and downstream of the magnet: $(x_0, y_0, z_0, \alpha_x, \alpha_y)$ and $(x_1, y_1, z_1, \beta_x, \beta_y)$ respectively. Performing MDF over the training sample yields an analytical fit function $P/Z^{mdf} = f(x_0, y_0, z_0, \alpha_x, \alpha_y, x_1, y_1, z_1, \beta_x, \beta_y)$, which can be applied to the positions and angles measured in the experiment.

In a similar way, a second MDF function for $\alpha_x$ angle was derived as $\alpha_x^{mdf} = g(x_0, y_0, z_0, \alpha_y, x_1, y_1, z_1, \beta_x, \beta_y)$. This function is used for the track-matching condition $(\alpha_x^{mdf} - \alpha_x)$=min, which allows to determine whether the tracks in upstream and downstream detection systems belong to the same global track through the magnet.

Having determined the two functions, $\alpha_x^{mdf}$ and $P/Z^{mdf}$, experimental data for the reference trajectory of unreacted $^{12}$C is used to adjust the input variables' offsets, which reflect the alignment of the real detectors in the experimental setup with respect to the magnetic field. This is achieved by variation of the offsets in the experimental input

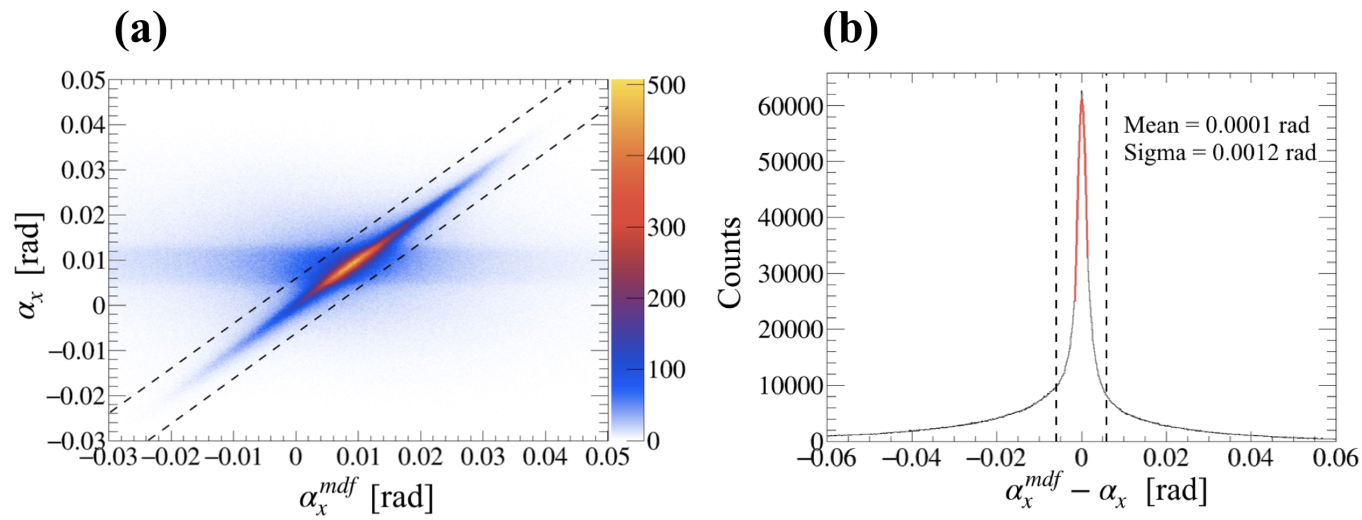


**Supplementary Fig. 1.** | **Track Matching.** (a) Correlation between $\alpha_x$ angle measured upstream of the magnet and the $\alpha_x^{mdf}$ reconstructed by the MDF. Dashed lines indicate applied cuts for the track matching condition. (b) Residual distribution $\alpha_x^{mdf} - \alpha_x$ and the applied cuts as in (a).

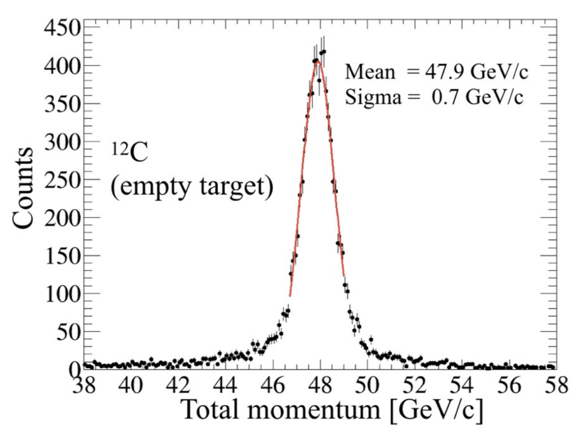


**Supplementary Fig. 2.** | **Fragment-Momentum Resolution.** Total momentum and its resolution for $^{12}$C measured with empty target.

variables simultaneously for $\alpha_x^{mdf}$ and $P/Z^{mdf}$ until the residual between $P/Z^{mdf}$ and its reference value is minimal. The reference value is chosen to be the $P/Z$ of unreacted $^{12}$C at the exit of the liquid-hydrogen target. Using this approach a total-momentum resolution of 0.7 GeV/c for $^{12}$C is achieved, as estimated with the empty target data, consistent with the resolution limits of the detection systems, see Fig. 2. The achieved momentum accuracy is evaluated to be 0.2%. Fig. 1 shows the performance of the second MDF function for $\alpha_x$. A global track is constructed when the reconstructed $\alpha_x^{mdf}$ falls within the $5\sigma$ gate indicated in the figure. In the analysis, only events with one global track, which combines the up- and downstream detectors, are considered (if not stated differently). In case of $^{11}$B and $^{10}$B only one charged-particle tracks are of interest. At this point we do not fully exploit the multi-track capability of this approach.

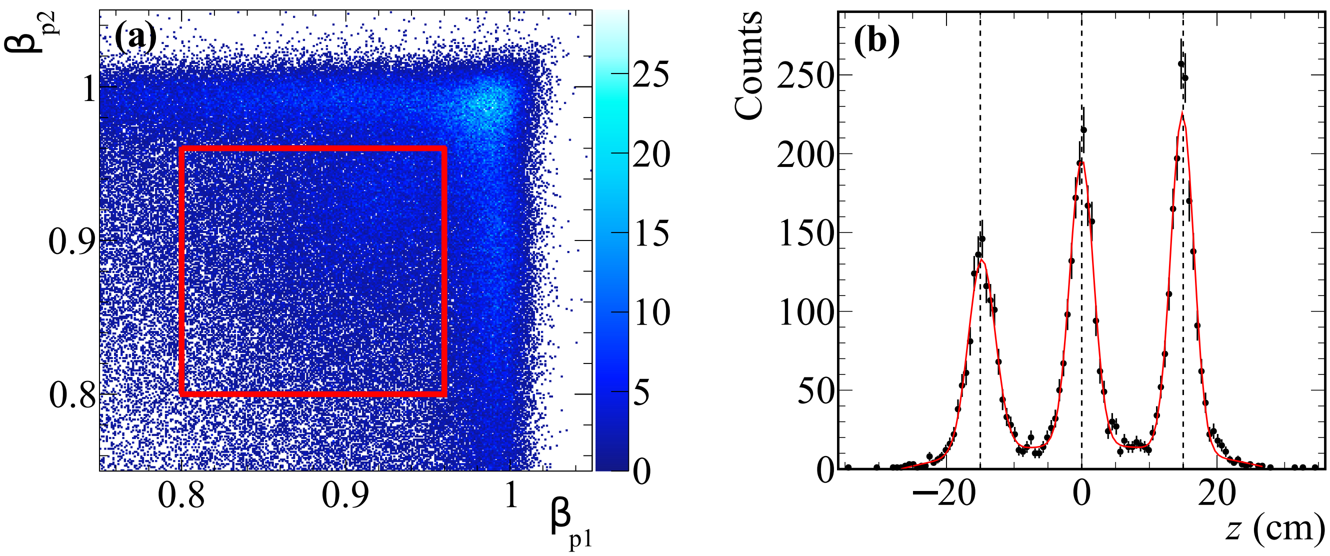


**Supplementary Fig. 3. | TAS Results.** (a) Basic velocity condition to select protons, the velocity cut in the left and right arm are indicated by the red lines. (b) $z$-vertex for 3 Pb foils at the target position to determine the position resolution of the vertex reconstruction. The position resolution is 1.8 cm ($1\sigma$), the fit is shown by the red line (plus background). The dashed black lines indicate the absolute position alignment at $z = \pm 15$ cm and zero.

The fragment tracking efficiency is $(55 \pm 5)\%$, obtained for an empty target run and given with respect to the an incoming and outgoing $Z = 6$ ion. This tracking efficiency includes the involved detector efficiencies, as well as the reconstruction and matching efficiency of good tracks. For the overall fragment identification efficiency an additional $(83 \pm 6)\%$ efficiency for the measurement of the outgoing charge needs to be added.

**3. Reaction-Vertex Reconstruction** The reaction vertex is reconstructed whenever one track is reconstructed in each arm of the TAS. This requires at least one hit in the GEM and RPC systems to form a linear track in each arm. We consider only single-track options from the hit combinations. The coincident two tracks that come closest, formed from all possible hit combinations, determine the vertex position along the beamline in the $z$ direction. Alignment procedures within the GEM-RPC system, the left and right arm, as well as relative to the incoming beam are applied. No particular reaction channel for absolute calibration purposes is available, therefore the detector positioning relies on a laser-based measurement, and the alignment relative to the other detector systems and the beam using experimental data. The quality of the tracks is selected according to their minimum distance, a selection criteria of better than 4 cm is applied in this analysis. Given the smaller angular coverage of the RPC system compared to the GEMs and detector inefficiencies, the track reconstruction efficiency is 40%, with an RPC detection efficiency of about 85%. The position resolution in $z$ was determined by placing three Pb foils separated by 15 cm at the target position. The reconstructed vertex position is shown in Fig. 3b, clearly three distinct peaks at a distance of 15 cm representing the Pb foils are reproduced. Given the width of each peak, the $z$-position resolution from the two-arm spectrometer is on average 1.8 cm ($1\sigma$).

Knowing the vertex and the position in the RPC, the flight length is determined. Together with the time-of-flight that is measured between the start counter BC2 and the RPC, the total momentum is determined. For the proton selection an initial velocity cut is applied, $0.8 < \beta < 0.96$, for each particle, see Fig. 3a. The absolute TOF calibration and internal time alignment for the RPC is done using a Pb target assuming that the signals arrive at the speed of light. The TOF resolution itself is determined by placing an additional thin Pb wall directly in front of the detector. Taking the subtracted TOF spectrum with and without the Pb wall, a signal from electron-positron production is measured. The TOF resolution, including the start timer, is about 175 ps.

[1] O. Hen, G. A. Miller, E. Piasetzky, and L. B. Weinstein, Rev. Mod. Phys. **89**, 045002 (2017).
[2] C. Ciofi degli Atti, Phys. Rept. **590**, 1 (2015).
[3] R. Cruz-Torres, D. Lonardoni, R. Weiss, N. Barnea, D. W. Higinbotham, E. Piasetzky, A. Schmidt, L. B.

Weinstein, R. B. Wiringa, and O. Hen, arXiv (2019), arXiv:1907.03658 [nucl-th].

[4] J. Kelly, Adv. Nucl. Phys. **23**, 75 (1996).

[5] R. Subedi *et al.*, Science **320**, 1476 (2008).

[6] A. Schmidt *et al.* (CLAS Collaboration), Nature **578**, 540–544 (2020).

[7] B. Schmookler *et al.* (CLAS Collaboration), Nature **566**, 354 (2019).

[8] F. Benmokhtar *et al.* (Jefferson Lab Hall A Collaboration), Phys. Rev. Lett. **94**, 082305 (2005).

[9] D. Rohe *et al.* (E97-006 Collaboration), Phys. Rev. Lett. **93**, 182501 (2004).

[10] L. Frankfurt, M. Sargsian, and M. Strikman, International Journal of Modern Physics A **23**, 2991 (2008).

[11] A. Tang *et al.*, Phys. Rev. Lett. **90**, 042301 (2003).

[12] E. Piasetzky, M. Sargsian, L. Frankfurt, M. Strikman, and J. W. Watson, Phys. Rev. Lett. **97**, 162504 (2006).

[13] I. Korover, N. Muangma, O. Hen, *et al.*, Phys. Rev. Lett. **113**, 022501 (2014).

[14] M. Duer *et al.* (CLAS Collaboration), Phys. Rev. Lett. **122**, 172502 (2019), arXiv:1810.05343 [nucl-ex].

[15] T. Kobayashi *et al.*, Nucl. Phys. A **805**, 431c (2008).

[16] V. Panin *et al.*, Phys. Lett. B **753**, 204 (2016).

[17] L. Atar *et al.*, Phys. Rev. Lett. **120**, 052501 (2018).

[18] O. Hen *et al.* (CLAS Collaboration), Science **346**, 614 (2014).

[19] G. Alkhazov, S. Belostotsky, and A. Vorobev, Phys. Rept. **42**, 89 (1978).

[20] E. O. Cohen *et al.* (CLAS Collaboration), Phys. Rev. Lett. **121**, 092501 (2018), arXiv:1805.01981 [nucl-ex].

[21] N. N. A. et al., in *Cryogenics 2019. Proceedings of the 15th IIR International Conference: Prague, Czech Republic, April 8-11, 2019.* (2019).

[22] M. Kapishin (BM@N), Nucl. Phys. A **982**, 967 (2019).

[23] "Conceptual design report bm@n — baryonic matter at nuclotron," ().

[24] S. Khabarov, E. Kulish, V. Lenivenko, A. Makankin, A. Maksymchuk, V. Palichik, M. Patsyuk, S. Vasiliev, A. Vishnevskij, and N. Voytishin, EPJ Web Conf. **201**, 04002 (2019).

[25] Y. Kovalev, M. Kapishin, S. Khabarov, A. Shafronovskaia, O. Tarasov, A. Makankin, N. Zamiatin, and E. Zubarev, Journal of Instrumentation **12**, C07031 (2017).

[26] V. Babkin *et al.*, Nucl. Instrum. Meth. A **824**, 490 (2016).

[27] "Bm@n daq system," ().